

Probabilistic Analysis of Turbine Blade Durability

by

Apostolos Koutras

B.S. Aeronautical/Mechanical Engineering
Hellenic Air Force Academy, 1991

Master in Business Administration (MBA)
National Technical University of Athens, Greece, 2003

S.M. Materials Science and Engineering
Massachusetts Institute of Technology, 2004

Submitted to the Department of Aeronautics and Astronautics
in Partial Fulfillment of the Requirements for the Degree of

Master of Science in Aeronautics and Astronautics

at the

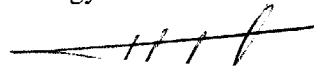
Massachusetts Institute of Technology

August 2004

[September 2004]

© 2004 Massachusetts Institute of Technology

All rights reserved



Signature of Author.....

Department of Aeronautics and Astronautics
August 20, 2004

Certified by

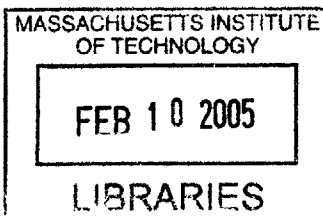
Edward M. Greitzer
H. N. Slater Professor of Aeronautics and Astronautics
Thesis Supervisor

Certified by

David L. Darmofal
Associate Professor of Aeronautics and Astronautics
Thesis Supervisor

Accepted by

Jaime Peraire
Professor of Aeronautics and Astronautics
Chair, Committee on Graduate Students



AERO 1

Probabilistic Analysis of Turbine Blade Durability

by

Apostolos Kountras

Submitted to the Department of Aeronautics and Astronautics
on August 20, 2004, in Partial Fulfillment of the
Requirements for the Degree of
Master of Science in Aeronautics and Astronautics

Abstract

The effect of variability on turbine blade durability was assessed for seven design/operating parameters in three blade designs. The parameters included gas path and cooling convective parameters, metal and coating thermal conductivity and coating thickness. The durability life was modelled as limited by thermo-mechanical low cycle fatigue and creep. A nominal blade design as well as two additional variants were examined using deterministic and probabilistic approaches. External thermal and pressure boundary conditions were generated by three-dimensional CFD calculations.

The location of expected failure was the bottom of the trailing edge cooling slot and was the same for all three designs examined. The nominal design had higher life and less variability for the ranges of design parameters examined. For the temperature range studied fatigue was the primary damage mechanism. The variation in cooling air bulk temperature was most important in setting the variation in blade durability life. This life variation was also affected by main gas bulk temperature and heat transfer coefficient, and cooling heat transfer coefficient, but to a lesser extent.

Thesis Supervisor: Edward M. Greitzer

Title: H. N. Slater Professor of Aeronautics and Astronautics

Thesis Supervisor: David L. Darmofal

Title: Associate Professor of Aeronautics and Astronautics

Table of Contents

Abstract	2
List of Illustrations and Figures	5
List of Tables	7
Acknowledgements	8
Nomenclature	8
1. Introduction	12
1.1 Background and Framework.....	12
1.2 Problem Description.....	13
1.3 Thesis Objectives	14
1.4 Overall Project Approach.....	14
1.5 Thesis Contributions	16
2. Blade Durability Life Approach	17
2.1 Durability Life.....	17
2.2 Fatigue Damage Estimate	19
2.3 Creep Damage Estimate.....	20
2.4 Concerns on the Durability Life Approach.....	24
3. Model Setup	27
3.1 Physical Part Description	27
3.1.1 Part Geometry.....	27
3.1.2 Part Material.....	30
3.2 Finite Element Modeling.....	32
3.2.1 Thermal Model	32
3.2.2 Structural Model.....	40
3.3 Probabilistic Analysis	46
4. Nominal Blade Analysis Results	49
4.1 Deterministic analysis	49
4.2 Probabilistic analysis.....	54
5. Blades -2 and -3 Analysis Results and Comparison	58

5.1 Deterministic analysis 58

5.2 Probabilistic analysis..... 63

6. Summary and Conclusions 66

6.1 Future Work Recommendations 67

Appendices 68

A. ANSYS Thermal Analysis 68

B. Structural Model Meshing..... 70

Bibliography..... 71

List of Illustrations and Figures

Figure 1 - Comparison of turbine hot components temperatures/stress with superalloys properties [2].....	12
Figure 2 - Project model general diagram	15
Figure 3 - Creep mechanisms map for pure Ni [2].....	21
Figure 4 - Typical creep strain vs. time plot for constant load & temperature [8]	22
Figure 5 - Creep strain rate vs. applied stress for IN-738LC @850°C [9].....	23
Figure 6 - Extrapolation of creep rupture data [8].....	25
Figure 7 – Blade-1 geometric model	27
Figure 8 - Blade internal cooling channels.....	29
Figure 9 – Blade tip crown and cooling channels exits.....	30
Figure 10 - Temperature dependent σ - ϵ curves for IN-738LC.....	32
Figure 11 - TBC coated surfaces in blade model (red-colored surfaces)	33
Figure 12 - CFD-generated h_f distribution	34
Figure 13 - ANSYS-mapped h_f distribution.....	34
Figure 14 - ANSYS thermal element SOLID90 [18].....	37
Figure 15 - Blade thermal model solid elements.....	38
Figure 16 - ANSYS thermal element SHELL131 [18]	38
Figure 17 - Thermal analysis output example	39
Figure 18 - CFD-generated pressure distribution.....	41
Figure 19 - ANSYS-mapped pressure distribution	41
Figure 20 - ANSYS structural element SOLID186 [18].....	42
Figure 21 - Structural model solid elements - general view.....	43
Figure 22 - Structural model solid elements - refined area in region of high stress and strain	43
Figure 23 - Maximum stress/strain location.....	44
Figure 24 - Cooling slot configuration	44
Figure 25 - Pre-cracked test specimen sketch	45
Figure 26 - Blade-1 PS metal temperature distribution.....	49
Figure 27 - Blade-1 SS metal temperature distribution.....	49

Figure 28 - Blade-1 PS equivalent stress distribution	50
Figure 29 - Blade-1 SS equivalent stress distribution	50
Figure 30 - Stress at Blade-1 life limiting location	50
Figure 31 - Blade-1 PS equivalent strain distribution	51
Figure 32 - Blade-1 SS equivalent strain distribution	51
Figure 33 - Strain at Blade-1 life limiting location	51
Figure 34 - Blade-1 durability life mapping.....	52
Figure 35 - Iso-stress temperature vs. time-to-creep-rupture plot for various superalloys [9]	53
Figure 36 - Blade-1 durability life distribution	54
Figure 37 - Normal distribution fitted in Blade-1 data.....	55
Figure 38 - "Low" life vs. general sample distributions for the seven input variables	57
Figure 39 - Metal temperature distributions in all three blade designs	58
Figure 40 - Equivalent (Von Mises) stress distribution in all three blade designs.....	59
Figure 41 - Equivalent (Von Mises) strain distribution for three blade designs	60
Figure 42 – Blade-2 durability life mapping	61
Figure 43 – Blade-3 durability life mapping	62
Figure 44 - Blade-2 durability life distribution	63
Figure 45 - Blade-3 durability life distribution	63
Figure 46 - Normal distribution fitted in Blade-2 data.....	64
Figure 47 - Normal distribution fitted in Blade-3 data.....	64
Figure 48 – Simplified 1-D heat transfer diagram.....	68

List of Tables

Table 1 - Selected design parameters approximate mean value.....	28
Table 2 - IN-738 mechanical and thermal properties.....	31
Table 3 - Probabilistic analysis input design parameters.....	47
Table 4 - Normally distributed random input variables.....	47
Table 5 – Blade-1 durability life distribution statistics.....	54
Table 6 - Blade-1 design input/output correlation coefficients.....	55
Table 7 – Blades -1, -2, and -3 durability life distribution statistics.....	63
Table 8 - Probabilities for "low" durability life.....	64
Table 9 - Variable inputs - durability life rank-order correlation coefficients.....	65

Acknowledgements

I would like to thank all the people who worked with and helped me on this thesis. Without their support the completion of this project would have been extremely difficult if not impossible. First, I would like to thank my thesis advisors Professors Edward Greitzer and David Darmofal for providing invaluable guidance throughout the project. My thesis research could have been very difficult to realize without the interest and support of MHI, Inc.; in particular, I would like to express my sincere thanks to Dr. Surao Aoki and Mr. Hideaki Sugishita of MHI for their support. I would like to also thank Dr. Yifang Gong of MIT/GTL who, as part of the research team, was always helpful with his remarks and suggestions.

For the accomplishment of my portion of the project we worked a lot with Jean Collins of MIT/Mech-E, who performed the aero-thermal part of it as his S.M. thesis; I am really in debt to him for his cooperation, friendliness and eagerness to assist me whenever needed. Also, I would like to express my thanks to Garrett Barter, graduate student of MIT/Aero-Astro, who provided invaluable support as computer administrator, as well as to Mr. Paul Warren, our computer/network manager in GTL and Ms. Julie Finn for her administrative support. Definitely, I need to thank my officemates Yong Wang and Matt Lackner for their friendship and support.

Last but certainly not least, I would like to really thank my wife Evanthoula and our children Vasiliki and Theofani for their uninterrupted support. Without their continuous encouragement this thesis and my whole course in Aero-Astro might have never been completed.

Nomenclature

d_c	Fractional damage due to creep
d_f	Fractional damage due to fatigue
Fh_{cool}	Cooling path heat transfer coefficient scaling factor
Fh_{gas}	Main gas path heat transfer coefficient scaling factor
h_{1-D}	Cooling path heat transfer coefficient as interpolated from 1-D calculations
h_{CFD}	Main gas path heat transfer coefficient as mapped from CFD calculations
h_{cool}	Cooling path heat transfer coefficient as applied to the FEM model
h_f	Heat transfer coefficient
h_{gas}	Main gas path heat transfer coefficient as applied to the FEM model
k_{metal}	Metal thermal conductivity
k_{TBC}	Thermal barrier coating thermal conductivity
l_{TBC}	Thermal barrier coating thickness
N	Durability life in cycles
N_f	Number of cycles to fatigue failure
Q	Material's diffusion activation energy
R	Boltzmann's constant
RA	Fracture area reduction
t_c	Cycle time
t_f	Time to creep rupture
T_{1-D}	Cooling path temperature as interpolated from 1-D calculations
T_{CFD}	Main gas path temperature as mapped from CFD calculations
T_{cool}	Cooling path temperature as applied to the FEM model
T_{gas}	Main gas path temperature as applied to the FEM model
T_m	Metal melting temperature

Greek

$\Delta\varepsilon_{tot}$	Total strain amplitude
ΔT_{cool}	Cooling path temperature offset factor
ΔT_{gas}	Main gas path temperature offset factor
E	Elasticity modulus
ε_c	Creep strain
ε_{cr}	Fracture critical strain
ε_{equiv}	Equivalent (Von Mises) strain
ε_f	True fracture ductility
ε_{tot}	Total strain
ρ	Spearman's rank-order correlation coefficient
ρ_{metal}	Metal density
σ_{equiv}	Equivalent (Von Mises) stress
σ_{tot}	Total stress
σ_{ult}	Material's ultimate strength
σ_y	Material's yield strength

Abbreviations

ASTM	American Society for Testing Materials
CAD	Computer Aided Design
CFD	Computational Fluid Dynamics
HCF	High Cycle Fatigue
FEM	Finite Element Method
LCF	Low Cycle Fatigue
LE	Leading Edge
LHS	Latin Hypercube Sampling
OEM	Original Equipment Manufacturer

TBC Thermal Barrier Coating
TE Trailing Edge
TMF Thermo-Mechanical Fatigue

1. Introduction

1.1 Background and Framework

Gas turbine performance depends critically on the maximum allowable engine firing temperature [1]. The adverse environment of high stresses at operating temperatures in the range of $0.7T_m$ (metal melting temperature) aggravated by corrosive factors leads to limitations in the life of the hot gas turbine components: combustors, turbine vanes, blades and disks. Currently, turbine parts are manufactured from nickel and cobalt-based alloys (*superalloys*), which provide a sufficiently high level of mechanical properties at elevated temperatures ($0.6T_m - 0.8T_m$).

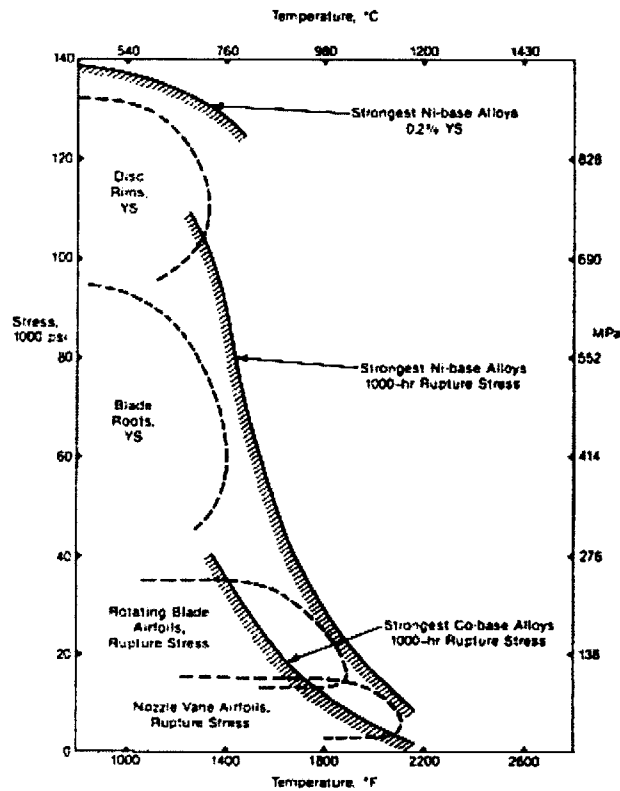


Figure 1 - Comparison of turbine hot components temperatures/stress with superalloys properties [2]

Figure 1 presents a comparative depiction of maximum loads experienced in gas turbine hot sections and superalloy mechanical properties limitations. There are a number of sources of loads imposed on turbine blades. Due to rotation, the blades are subject to centrifugal

stresses ranging from 10,000 psi in industrial turbine first-stage blades to 40,000 psi at the airfoil root of highly cooled aircraft turbines [2]. Superimposed on this is the stress created by the pressure difference from pressure to suction side of the blade. The application of these stresses in the blade metal under temperatures often exceeding 800°C results in *creep* being a primary concern in the design of turbine blades. Internal air cooling is used to extend blade creep life. The cool air passing through the blade results in local hot/cool spots within the metal that lead to thermal straining of the material. Sequential engine start-ups and shutdowns create time-varying thermo-mechanical loads, which can lead to *low-cycle fatigue* (LCF). Thermo-mechanical fatigue has been identified to be the controlling failure mode of aircraft turbine blades [2].

As the blades rotate with the disk, they pass through non-uniformities created by preceding engine parts (nozzle, combustor, vanes etc). The periodic variation of force creates *high-cycle fatigue* (HCF) loading.

Often, the air and fuel mixture passing through gas turbines contains levels of sodium, potassium, vanadium, and lead that enter into the sulfidation process and cause blade material corrosion. Corrosion-resistant alloys and specific barrier coating applications are used to inhibit corrosive attack to blade metal, but environmental degradation decreases the material resistance to creep and fatigue and lowers the overall blade durability life.

1.2 Problem Description

Estimation of blade durability life is usually performed at a late stage of the blade design process when many parameters have already been set and a need exists to establish tools and methodology for the life assessment early in the design process. In addition, there is variability in thermo-mechanical design parameters and in operating conditions which lead to variability in blade durability life. A preliminary design method should not only be fast and agile enough to be implemented during early design stages but also be able to accurately capture the dependence of blade durability on parameters variability.

A step in establishing such a method is developing an insight into the durability life variability and sensitivity to the uncertainty in blade design/operating parameters.

1.3 Thesis Objectives

The present thesis project objectives can be summarized as follows:

- a. Assess the durability life of three (3) turbine blade designs.
- b. Calculate the variability of the durability life for these blades as a result of design/operating parameter uncertainty.
- c. Define the sensitivity of the durability life to design/operating parameter uncertainty by identifying those parameters that lead to the most variability in life.

1.4 Overall Project Approach

Three (3) different configurations of a particular turbine blade design were analysed. A turbine engine OEM (Mitsubishi Heavy Industries Inc.) provided the three designs, intending to span a significant portion of the design space, with respect to the anticipated durability life. The first design (hereafter referred to as *Blade-1*) was provided as the baseline (nominal) blade configuration. For all three versions the same approach was used, as detailed in the present section.

For the purpose of durability life estimation only the combined effects of LCF and creep were considered and modelled. It is recognized that environmental degradation (oxidation) contributes to the acceleration of primary failure mechanisms and that HCF can be a contributor to failure. The initial step taken here, however, was to model durability life as being limited by only LCF and creep.

As it is detailed in Chapter 2, expected durability life can be assessed as a direct function of the stress and strain experienced by the blade at a specific location. Figure 2 provides a general schematic of the methodology that was followed.

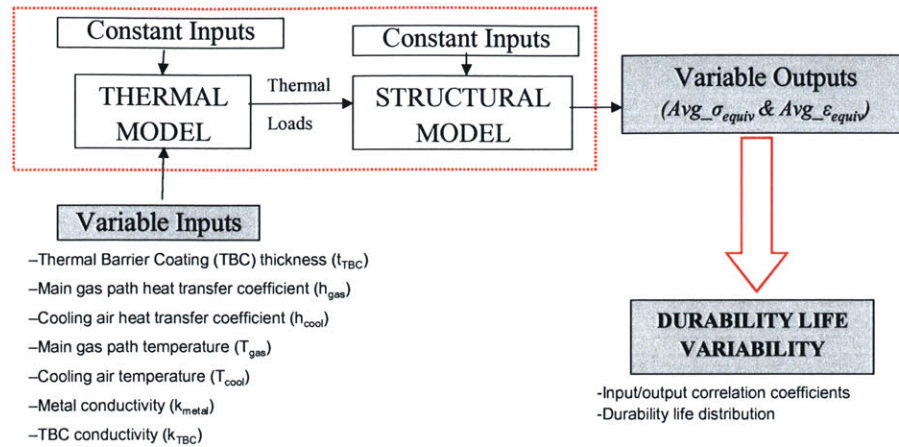


Figure 2 - Project model general diagram

The overall blade analysis involved two sub-models: thermal and structural. Both were applied using ANSYS¹ finite element method (FEM) software. In the thermal sub-model, the blade geometry was modeled and heat convection boundary conditions were applied for the main gas path surfaces as well as for the internal cooling passages.

The thermal load estimated from the thermal sub-model was used as boundary condition in the structural sub-model with the addition of the following conditions: pressure loads on the pressure and suction sides of the airfoil, centrifugal loads due to blade rotation, and no-displacement of the blade lower part were also applied. The results of the structural sub-model included the total stress and total strain at all locations of the blade. Further details are provided in Chapter 3.

The durability life of all the FEM solution points (nodes) were calculated based on total stress/strain value and the most critical blade location was identified based on lowest durability. A single durability life value was thus attributed to a given blade.

To estimate the effect of variability of the selected parameters in the blade durability, probabilistic analysis was performed. For this, 1000 thermal/structural model simulations were run for each of the three different blade configurations. The result was a

¹ ANSYS Inc, 275 Technology Dr., Canonsburg, PA 15317, <http://www.ansys.com>

distribution of durability life, as well as its sensitivity to the variable inputs (selected design parameters) in terms of rank-order correlation coefficients.

1.5 Thesis Contributions

The contributions of the thesis are:

- a. The development (with the work carried out in [3]) of a framework for the end-to-end aero-thermo-structural analysis of turbine blades.
- b. The assessment of the impact of design parameter uncertainty on the variability in durability life.

2. Blade Durability Life Approach

2.1 Durability Life

Turbine blade durability life is limited by a number of factors, which, either by themselves or by interaction with each other, can result in degradation of its capacity to withstand service-induced stresses to a level that the part cannot reach the designed performance, and – even worse – possibly fail during service. The durability limiting problems can be generally categorized as *mechanical property related*, *corrosion related* or *service degradation related*. Most field durability problems involve factors belonging to more than one category [4].

From the purely mechanical perspective, the damage mechanisms include fatigue (LCF, HCF, and thermal fatigue), creep, and their interaction. The combination of mechanical (LCF and/or HCF) and thermal fatigue is generally referred to as *thermomechanical fatigue* (TMF). In present analysis, durability life was assessed from the perspective of the combined effect of TMF and creep, based on information about the importance of TMF/creep mechanism which is known to be a primary mechanism of turbine blade failure [2].

Blades located in the hot gas path of land-based engines turbine section are also subject to a combined oxidation-sulfidation phenomenon, usually referred to as *hot corrosion*. Air and fuel elements entering the sulfidation process attack the blade base metal and cause corrosion of the blade airfoil. Damage mechanisms involve not only the metal mass waste but also the corrosion-induced degradation of the material's baseline mechanical properties. Several mechanisms through which hot corrosion negatively influences material resistance in high temperature fatigue have been described [5]. These basically concern the microstructural aspect of fatigue resistance and its implications due to oxidation (e.g. cavities/crack closure prevention, initiation of micro-cracks due to preferential oxidation attack at grain boundaries, etc). Coatings are the primary defence against corrosion. Hot corrosion was not included in this initial stage of the project².

² It might be expected that the thermal barrier coating on the main gas path surfaces of the blade was modelled only from its thermal resistance perspective.

Numerous approaches exist to predict failure life of engineering materials subjected to elevated temperature fatigue where creep is a significant life-limiting factor. The most widely used methods can be classified into the following three groups: (i) damage accumulation models, (ii) frequency-modified Coffin-Manson equations, and (iii) strain range partitioning [5]. A linear damage accumulation model was used in this work both because of its convenience for use in the required modelling framework (modelling of a full 3-D part, accommodation of high number simulations for probabilistic analysis etc) and also because the primary objective of the study was the identification of life variability – sensitivity rather than the precise durability life estimate.

In linear damage accumulation method, the damage accumulated by mechanical fatigue and creep are linearly superposed, such that

$$d_f + d_c = 1 \quad (1)$$

where d_f and d_c are the fractional damage due to fatigue and creep, respectively [5]. If a part is subjected to N fatigue cycles under strain amplitude $\Delta\epsilon_{tot}$, and the material number of cycles to failure at this strain amplitude is $N_f(\Delta\epsilon_{tot})$, the fraction of the damage due to fatigue only is given by $N/N_f(\Delta\epsilon_{tot})$. Similarly, if t_{creep} is the time that a part is under stress level σ_{tot} and $t_f(\sigma_{tot})$ is the time to creep rupture at this stress level, the fraction of damage attributed to creep only would be $t_{creep}/t_f(\sigma_{tot})$. In the present study, it was assumed the overall life of the blade is comprised of N cycles of cycle-time $t_c=14$ hr each. Thus $t_{creep}=N \cdot t_c$ and Equation (1) can be written, with N being the required durability life in number of 14-hr cycles, as:

$$\frac{N}{N_f(\Delta\epsilon_{tot})} + \frac{N \cdot t_c}{t_f(\sigma_{tot})} = 1 \quad (2)$$

The linear damage model is valid when the interaction between fatigue and creep damage is restricted to the actual event of failure [6]; in other words, the sum of the terms in Equation (2) is unity at failure if the weakening of the load bearing part section by fatigue and creep driven mechanisms is additive. When the failure occurs by one

mechanism only, without aggravation by the other, the sum of terms in Equation (2) can be as high as two. On the other hand, if the underlying damage mechanism of one cause (e.g. creep) is substantially accelerated by the other (e.g. creep cavitation damage being accelerated by excess voids created by cyclic fatigue loads), the failure happens earlier than predicted by Equation (2) and the sum of terms is less than one. For the scope of the present study, with microstructural damage modelling not part of the project objectives, Equation (2) has been adopted with the assumption that no such interaction of fatigue and creep occurs. It is recognized, however, that this is an approximation and that as the temperature increases the interaction becomes more important [4, 5].

2.2 Fatigue Damage Estimate

In engineering materials fatigue failures often occur as a result of application of cyclic stresses at levels usually much lower than the uniaxial tensile strength of the material. High-cycle fatigue occurs at high frequencies associated with resonant vibrations of the blade as a result of the air stream disturbances. In general, stresses during HCF are low and therefore only elastic deformation mechanisms apply [4]. In the present study the effects of HCF were not addressed.

Low-cycle fatigue occurs as the result of applied loads once per each engine operating cycle. In the present case, the amplitude and frequency of the load are assumed constant throughout the whole life of the part, the period of the cyclic load being $t_c=14\text{hr}$. Such loads typically involve thermal expansion of the blades between engine start-up and shutdown in conjunction with the centrifugal load due to blade rotation. The level of the total applied loads is generally of the order of the material yield strength. This was also confirmed in the present study.

For many engineering applications, turbine blades undergo a combination of elastic, unconstrained deformation with localized plastic flow, particularly at locations of stress concentrations [4, 5]. Therefore, it was decided to use the strain-life approach for fatigue life calculation as expressed by the combined Coffin-Manson & Basquin relation [5]:

$$\frac{\Delta \varepsilon_{tot}}{2} = \frac{\sigma_f'}{E} \cdot N_f^b + \varepsilon_f' \cdot N_f^c \quad (3)$$

where σ_f' is the fatigue strength³ and ε_f' the fatigue ductility coefficients. The first and second terms on the right hand side of Equation (3) are the elastic and plastic components, respectively, of the total strain applied ($\Delta \varepsilon_{tot}$). By solving Equation (3) for N_f one can find the required number of cycles to fatigue failure, under the given strain amplitude $N_f(\Delta \varepsilon_{tot})$, which is needed for durability life estimate (Equation (2) in previous section). In a more practical form Equation (3) is referred to as *the universal slopes method* and described [7] by:

$$\Delta \varepsilon_{tot} = \frac{3.5 \cdot \sigma_{ult}}{E} \cdot N_f^{-0.12} + \varepsilon_f^{0.6} \cdot N_f^{-0.6} \quad (4)$$

where,

- σ_{ult} : Ultimate strength
- E : Elasticity (Young's) modulus
- ε_f : True fracture ductility = $\ln \frac{1}{1 - RA}$
- RA : Fracture area reduction

Equation (4) with the noted coefficients⁴ was used for estimate of the fatigue damage and subsequently, through Equation (2), for durability life calculation.

2.3 Creep Damage Estimate

Creep is a time-dependent, thermally-activated deformation under stress. Although several theories describe creep mechanisms, these can be categorized in two basic groups [2]: (i) defect-free flow which happens when theoretical shear strength limit is exceeded, and (ii) material deformation due to defects in the microstructure (dislocations, point

³ To a good approximation σ_f' is equal to the true fracture strength, corrected for necking, in a monotonic tension test for most metals.

⁴ They concern material properties from monotonic, uniaxial tests.

defects, grain boundary flaws, etc). Figure 3 demonstrates the creep mechanisms map for pure Ni (representative of superalloys), in a plot using normalized tensile stress (stress divided by shear modulus) versus homologous temperature (operating temperature divided by material melting point).

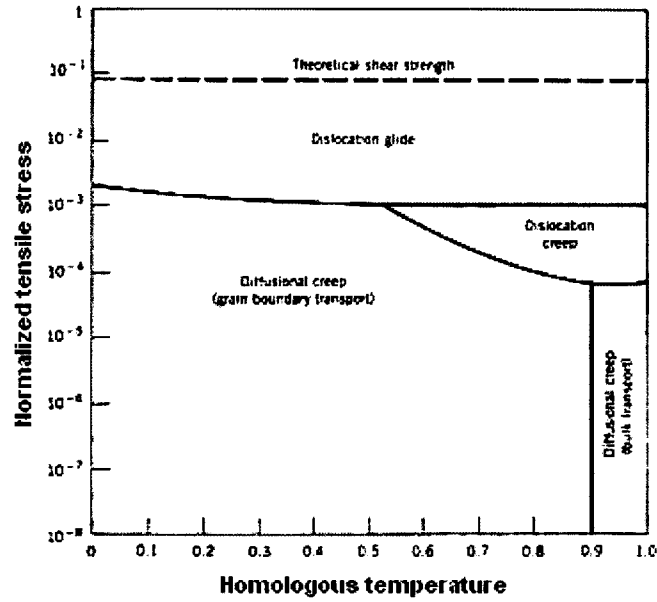


Figure 3 - Creep mechanisms map for pure Ni [2]

The defect-related mechanisms require high-temperature to activate the defects. This is the case in turbine blades where, usually, the metal operating temperatures are $0.6T_m$ - $0.7T_m$ or more [2] and creep is a significant factor in blade life. As seen in Figure 3 different creep mechanisms occur in this temperature range, depending on stress level. This presented a modeling issue as detailed below.

Creep-induced deformation is typically presented in terms of strain, called *creep strain* (ϵ_c). Figure 4 provides a typical creep strain – time plot.

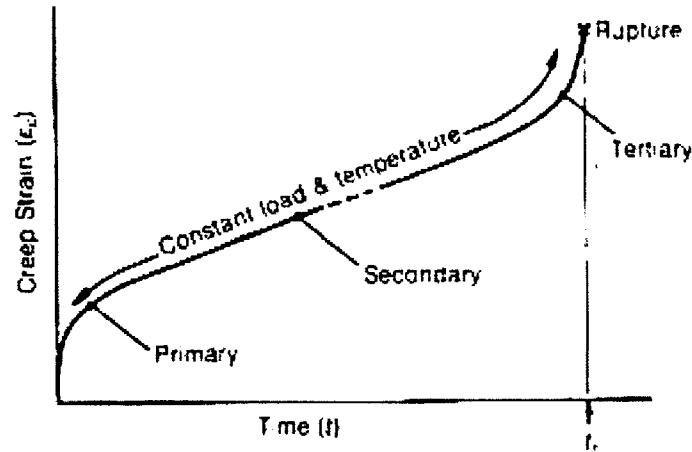


Figure 4 - Typical creep strain vs. time plot for constant load & temperature [8]

Three distinct creep regions can be noted in the diagram: primary, secondary, and tertiary where actual rupture is anticipated. Although several approaches exist for modeling of primary and even tertiary creep stages, only secondary stage (steady-state) is modeled here, since it occupies the significantly larger portion of “creep life” and the modeling could be accommodated with minimum complications.

Various phenomenological and empirical approaches have been proposed to model secondary creep [8], by expressing the relation between applied stress, operating temperature and creep strain. One of them is Norton’s law which models the creep strain rate as [9]:

$$\dot{\epsilon}_c = A \cdot \sigma_{tot}^n \cdot e^{-\frac{Q}{R \cdot T}} \quad (5)$$

where,

- σ_{tot} : Total applied stress
- A, n : Material coefficients
- Q : Material diffusion activation energy
- T : Operating temperature
- R : Boltzmann’s constant

Due to the various creep mechanisms which are active at different points in the $\sigma_{tot} - T$ space (Figure 3), the exponent n is not constant for the analyzed blade material (IN-738LC) [9].

A simplified version of Norton's law is given in [9]. Due to lack of temperature-dependent creep strain rate data for the model material (IN-738LC) equation (5) was expressed as:

$$\dot{\epsilon}_c = B \cdot e^{C \cdot \sigma_{tot}} \quad (6)$$

where B and C are empirical coefficients. According to Hoffelner [9] their values are $B=1.5 \times 10^{-11} [\text{sec}^{-1}]$ and $C=2.5 \times 10^{-8} [\text{Pa}^{-1}]$. As seen in Figure 5 coefficients B and C refer to IN-738LC superalloy at 850°C . Although this temperature did not apply to all blade locations in the project, it characterizes the most critical conditions and Equation (6) was used with the above mentioned coefficients assumed constant.

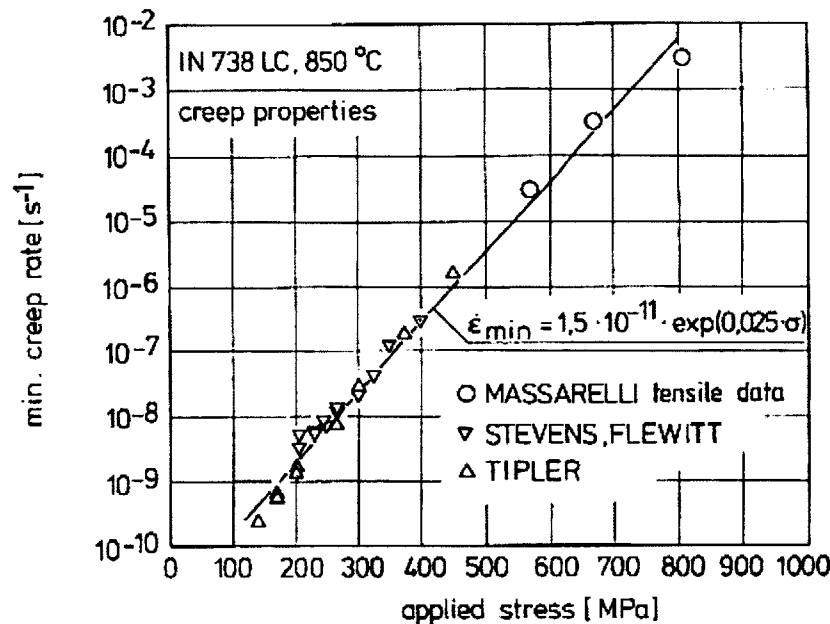


Figure 5 - Creep strain rate vs. applied stress for IN-738LC @850°C [9]

Equation (6) was incorporated in the FEM model for the 14-hr cycle analysis as well the post-FEM-solution processing for the calculation of time to creep rupture $t_f(\sigma_{tot})$. It was assumed that applied stress σ_{tot} would be constant from the end of one cycle until creep rupture. To calculate the time to creep rupture Equation (6) was solved with σ_{tot} , B and, C

assumed constants. For rupture creep strain, the value of $\varepsilon_{cr}=0.07$ was used, based on the material's (IN-738LC) uniaxial test data [10].

2.4 Concerns on the Durability Life Approach

The subject of crack initiation and propagation until failure in elevated temperatures is a complex topic [5] due to the nature of high-temperature fatigue as a combined result of creep, cyclic loading, and environmental corrosion. In the context of the present project, the modeling must capture the effects of the primary damage mechanisms in a turbine blade, while keeping the overall model efficient enough to be used in the multiple runs necessary for the probabilistic analysis. The study did not require a highly accurate durability life estimate, but rather was focused on assessing the differences in the durability variability for different blade designs. With three fairly similar blades, any inadequacy of the model should affect the analyses in a similar manner. However, the model is far from complete, and this section presents some issues and concerns to be considered in possible future use of the project results.

Equation (4) that is used for calculation of the fatigue damage is quite general. It captures the basic phenomenon and it has found widespread application in industrial practice [5]. However, it does not consider several conditions that have an effect on crack propagation (crack closure mechanisms, plasticity, actual scheme of cyclic loading, etc). In addition, the approximation assumes a “defect-free” material where the crack initiation time may account for a large proportion of the overall life (from 0% to 80%) [5]. In actual parts conditions may not be “defect-free”.

Equation (6) for time-to-creep-rupture is also general and empirical. As most models used in practice, it is intended to extrapolate rupture data from relatively limited portion of the load/temperature/time space (usually from short time experiments at high stress levels [9]) and to estimate rupture time of an actual component. The level of uncertainty in the approach is shown in Figure 6 [8]. For a stress level of 170 MPa, the difference in creep damage estimate may be as high as a factor of 2.

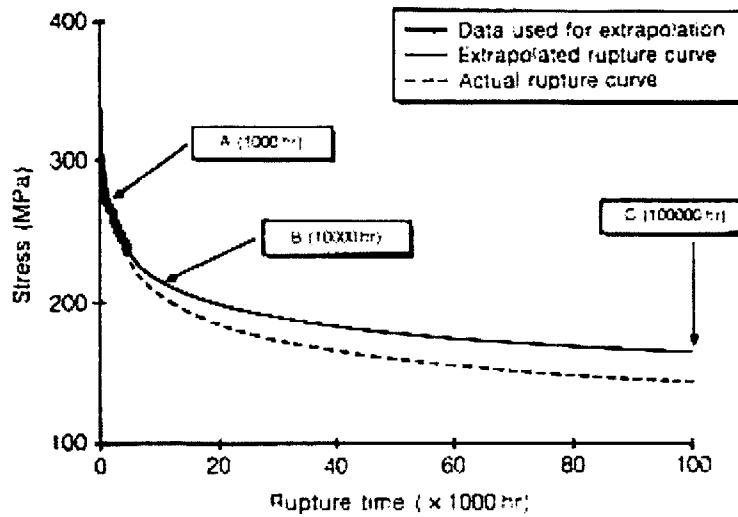


Figure 6 - Extrapolation of creep rupture data [8]

This inherent uncertainty in the extrapolation of creep data is to a large extent attributed to the fact that the creep data used do not necessarily correspond to the same creep mechanism regions as the ones through which the material actually proceeds before reaching creep rupture state [8]. Thus, the use of a particular creep model equation may not capture the actual micromechanisms in creep formulation for a given application.

Additionally, the use of constant stress after the end of the 14hr cycle (as calculated by ANSYS structural model) is conservative, as it does not account for the phenomenon of *stress relaxation* that is known to exist in creep. Other studies [6] have shown that taking or not this phenomenon into consideration could lead to different estimates of IN-738LC lives within a factor of 4.

Stress rupture data used to estimate fatigue life in Equation (4) are derived from monotonic load tests which are not, in general, representative of the combined creep-fatigue behavior encountered in a high temperature environment. Further, the uniaxial material properties used for fatigue formulation may be inaccurate due to the fact that they were used isotropically, without accounting for the direction of cracking and similar anisotropic effects. Crack orientation relative to the material crystal and/or grain orientation have significant impact on fatigue life calculation; Ni-based superalloys are known to have the best fatigue properties in certain crystallographic directions [2]. Orientation of these axes

with the airfoil cross-sectional axes could become a considerable factor in durability life estimate.

To summarize, the fatigue/creep model used is a conventional approximation applied to make prediction and probabilistic analysis of turbine blade durability life.

3. Model Setup

3.1 Physical Part Description

3.1.1 Part Geometry

The blades analyzed are first stage rotor blades of a land-based turbine engine. As noted previously, geometric models for the nominal configuration (*Blade-1*) and the two variants (*Blade-2* and *Blade-3*) were provided by the engine OEM. Figure 7 provides a view of the nominal blade geometry.

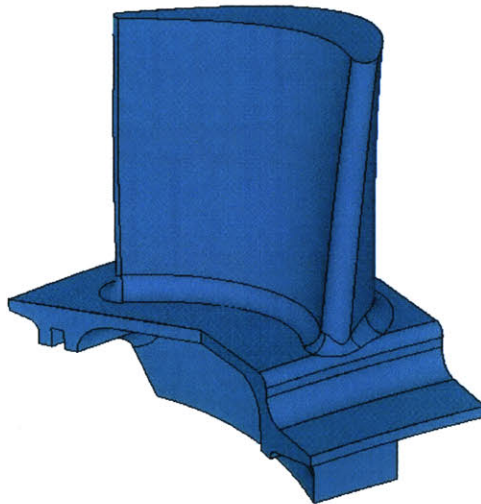


Figure 7 – Blade-1 geometric model

Detailed design parameters of the blade are not provided herein; however Table 1 summarizes the relation of particular design parameters in Blade-2 and Blade-3, with respect to Blade-1 values. These design parameters were assumed to be *controllable* and were unchanged throughout the probabilistic analysis of the specific design configurations.

	<u>CONTROLLABLE PARAMETER</u>	<u>Blade-1</u> (nominal)	<u>Blade-2</u>	<u>Blade-3</u>
a.	Pitch/Chord ratio (axial)	1	0.9	1.1
b.	Maximum blade thickness (mm)	1	0.9	1.1
c.	Leading edge radius (mm)	1	1.1	0.9
d.	Trailing edge radius (mm)	1	1.1	0.9
e.	Leading edge wedge angle (deg)	1	1.1	0.9
f.	Trailing edge wedge angle (deg)	1	1.1	0.9

Table 1 - Selected design parameters approximate mean value

All blade surfaces in contact with main gas path (airfoil, tip and platform upper surface) were modeled as being coated with a protective thermal barrier coating (TBC) of nominal thickness (l_{TBC}) equal to 0.3mm.

The internal cooling channels are shown in Figure 8. The characteristics of these channels are:

- a. Straight channel (*Channel-A*) along the LE, ending in a round hole at the blade tip through which cooling air flows outward.
- b. Serpentine channel (*Channel-B*) that spans approximately from 15% to 60% chordwise, ending in a trapezoidal shaped hole at the blade tip.
- c. Cooling bay (*Channel-C*) occupying the internal blade volume from 60 % to 100% chordwise, which ends in a slot along the blade TE, through which cooling air flows outward.

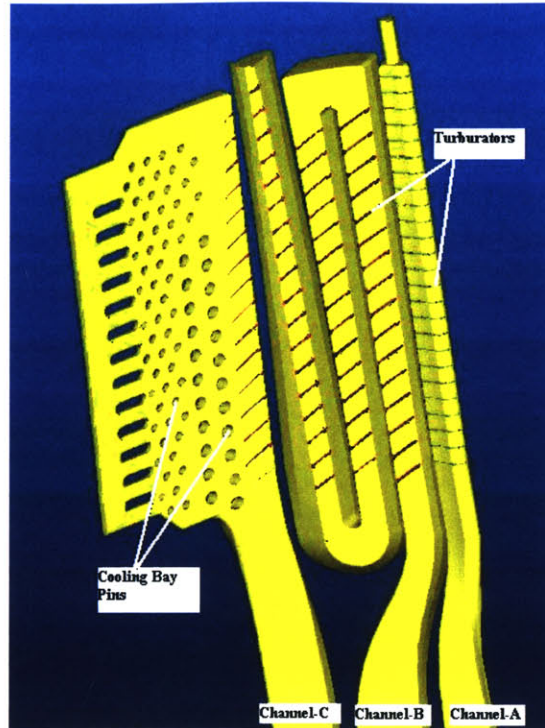


Figure 8 - Blade internal cooling channels

Figure 8 shows that along the cooling channels there are series of turbulators (small protuberant ribs used to increase heat transfer between metal and cooling air) located perpendicular to the airflow. Similarly, in cooling channel C there are turbulators as well as pins connecting the two opposing faces of the bay.

The detailed blade geometry models for all three configurations were received from the OEM in the form of CAD Pro/Engineer⁵ files and transferred to ANSYS using an ANSYS-Pro/Engineer connection software module. The models included all geometric features of the blades including turbulators and pins. As described in ANSYS documentation [11], it was deemed necessary to remove from the geometric model certain small features (model “*defeaturing*”) to eliminate problems with meshing. The geometry used in the FEM analyses did not thus include the following features:

- i. Cooling channels turbulators.
- ii. Cooling bay pins.
- iii. Cooling channel cross-section rounded corners.

⁵ PTC Worldwide Headquarters, 140 Kendrick St., Needham, MA 02494, <http://www.ptc.com>

- iv. Film cooling holes in the airfoil surfaces.
- v. Cooling channels exit holes in the blade tip (see Figure 9).
- vi. “Crown” shaped barrier along blade tip periphery (see Figure 9).

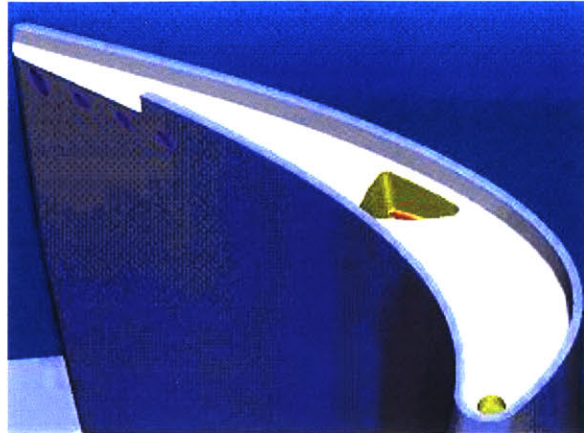


Figure 9 – Blade tip crown and cooling channels exits

3.1.2 Part Material

The material used for blade model was the nickel-based IN-738LC superalloy, a heat treatable cast alloy with substantial high-temperature strength and satisfactory levels of ductility, fracture toughness, and fatigue resistance [10]. IN-738 presents higher resistance to hot corrosion than its predecessor (superalloy IN-713C). It is used primarily in elevated temperatures/high-loads applications such as gas turbine blades, vanes, and integral disks. A slightly modified version of the alloy, designated IN-738LC, has lower carbon and zirconium contents for improved castability and only minor effect on mechanical properties. In the present study wherever it was not possible to locate IN-738LC properties, the respective values for IN-738 superalloy were used. The mechanical and thermal properties used are summarized in Table 2. All properties were assumed to be isotropic.

	<u>PROPERTY</u>	<u>SYMBOL</u>	<u>VALUE</u>	<u>SOURCE</u>
a.	Thermal conductivity	k_{metal}	18 W/m·K	[12]
b.	Density	ρ_{metal}	8110 Kgr/m ³	[13]
c.	Mean coefficient of thermal expansion	α	11.6x10 ⁻⁶ K ⁻¹	[13]
d.	Modulus of elasticity (Young's)	E	1.75 GPa	[12]
e.	Poisson's ratio	ν	0.3	assumed
f.	Melting point	T_m	1230 – 1315 °C	[12]
g.	Yield strength	σ_y	1000 MPa	[12]
h.	Area reduction at fracture	RA	10%	[10]
i.	Ultimate strength	σ_{ult}	1095 MPa	[12]
j.	Strain at fracture	ϵ_{cr}	7%	[10]

Table 2 - IN-738 mechanical and thermal properties

As most common engineering materials, the material modeled (IN-738LC) does not have an elastic-only behavior, especially in the high-temperature/high-stress applications of turbine blades. It exhibits a linear stress-strain relationship up to the *proportional limit*, beyond which it becomes nonlinear. Figure 10 provides the stress – strain relations used for the particular material, IN-738LC [14, 15].

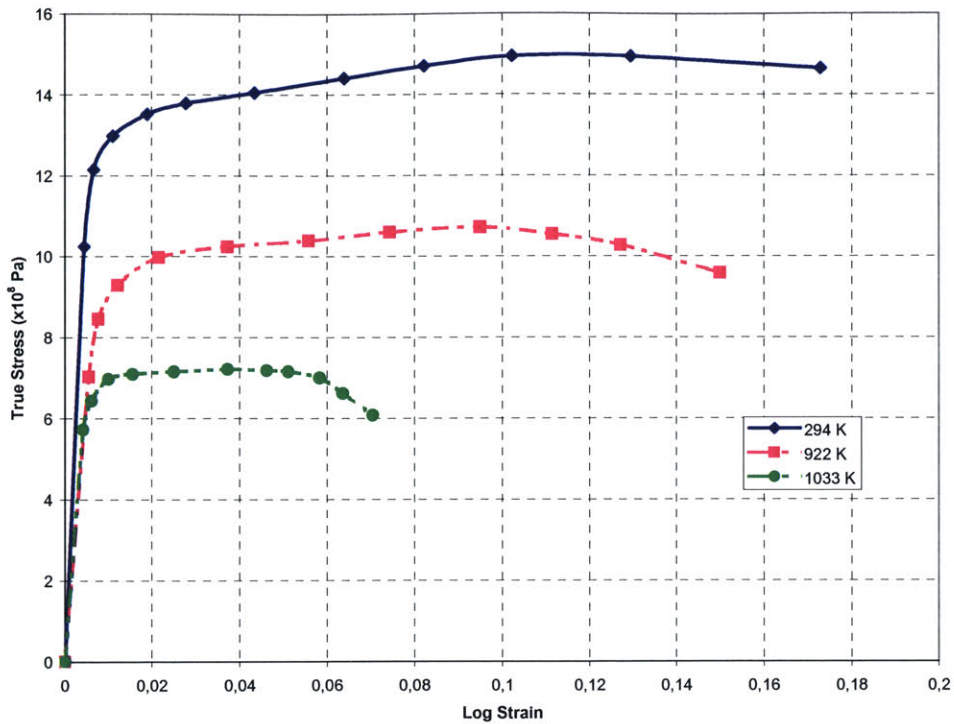


Figure 10 - Temperature dependent σ - ϵ curves for IN-738LC

3.2 Finite Element Modeling

As noted previously, the FEM model consisted of two interconnected (thermal and structural) sub-models. The results of the thermal sub-model (metal temperature distribution) were used as inputs to the structural calculation. The following paragraphs describe the features of the sub-models.

3.2.1 Thermal Model

The inputs to the thermal model were the following:

- a. Thermal properties of the materials.
- b. Gas path thermal boundary conditions.
- c. Cooling path thermal boundary conditions.
- d. Thermal boundary conditions for other surfaces, not in the main gas path or the cooling channels.

The thermal properties of the metal continuum were presented in Section 3.1.2 previously. The blade surfaces that were exposed to the main gas path (airfoil, tip, hub platform top) were modeled as coated with a TBC material of nominal thickness equal to 0.3mm, with isotropic thermal conductivity $k_{TBC}=1$ W/m·K [16]. Figure 11 provides a view of the TBC-coated blade surfaces.

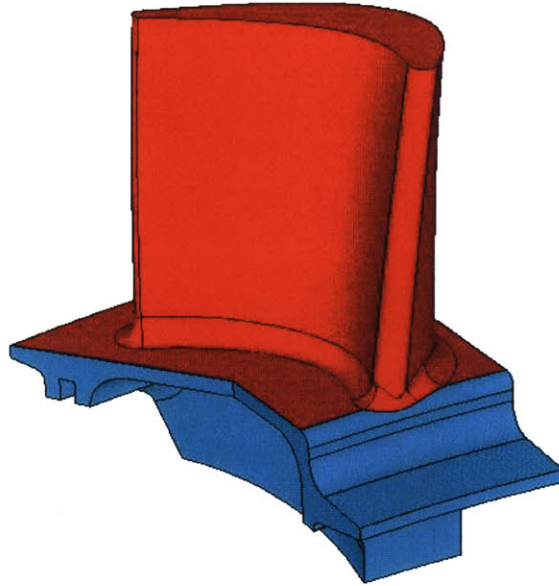


Figure 11 - TBC coated surfaces in blade model (red-colored surfaces)

The main gas path thermal boundary conditions were modeled as convective heat transfer loads, using heat transfer coefficient (h_{gas}) and bulk (adiabatic wall) temperature (T_{gas}) at several points of the TBC-coated surfaces, and in particular at the centroid point of each one of the TBC-coated surfaces elements. The heat transfer coefficient and temperature values were obtained from three-dimensional CFD calculations performed as a separate part of the present overall project [3]. The effect of film cooling was modeled based on experimental data for cases with similar geometries [3]. The adiabatic wall temperature obtained from this modeling, and the heat transfer coefficient values for each point of the CFD grid, constituted the input boundary conditions for the FEM thermal sub-model.

The CFD-generated boundary conditions were transferred to the FEM model using ANSYS mapping capability (MOPER command) [17]. ANSYS calculates the values of the

given parameters (T_{gas} and h_{gas}) for the desired points (ANSYS model surface element centroids) by interpolating the values of the parameters at the three closest points of the CFD grid. The geometries in the CFD and FEM models were not exactly the same, since the CFD-used geometry was built separately whereas the FEM-used geometry was imported from Pro/Engineer files. Nevertheless, the mapping operation transferred the CFD results to ANSYS with a satisfactory accuracy as can be noted in the heat transfer coefficient distributions in Figure 12 and Figure 13 below. (The actual heat transfer coefficient values have been normalized with respect to the maximum CFD-generated h_f value.)

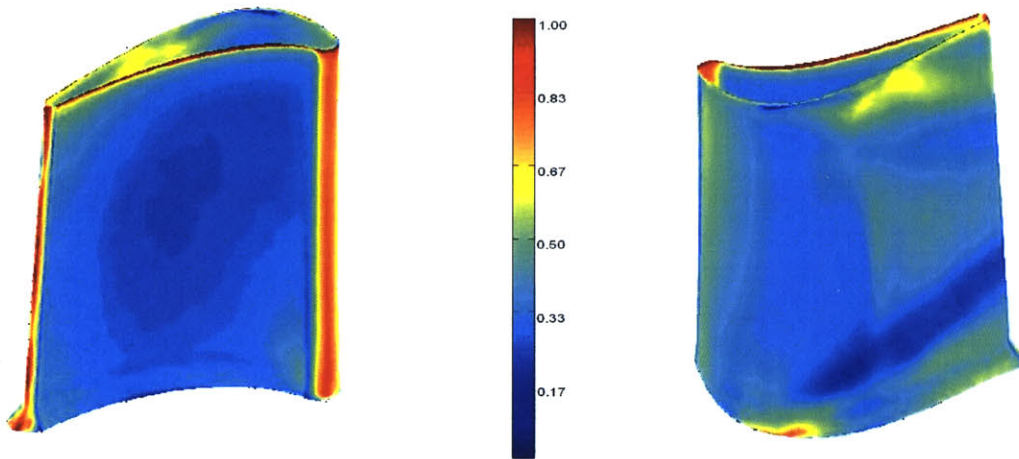


Figure 12 - CFD-generated h_f distribution

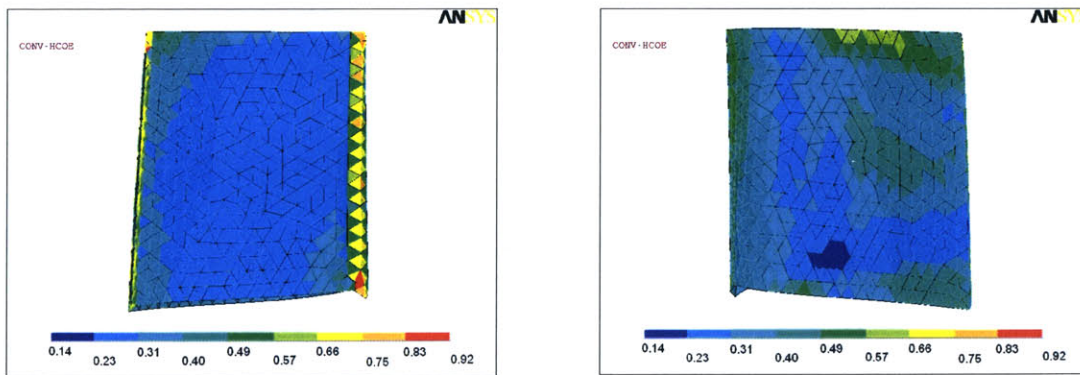


Figure 13 - ANSYS-mapped h_f distribution

The gas path convective heat transfer parameters were designated noise variables for the durability life study. The CFD-generated data for each blade version were thus used

as the baseline, with their variability described using scaling and an offset factors for h_{gas} and T_{gas} , respectively. In particular, for the gas heat transfer coefficient the following equation was used:

$$h_{gas} = h_{CFD} \cdot Fh_{gas} \quad (7)$$

where,

- h_{gas} : main gas path heat transfer coefficient applied to the model
- h_{CFD} : main gas path heat transfer coefficient mapped to ANSYS model points from CFD calculations
- Fh_{gas} : main gas path heat transfer coefficient scaling factor; its nominal value was 1 and, as detailed in section 3.3, it followed a probabilistic distribution function in order to model the gas path heat transfer coefficient variability

For the gas path temperature, the following equation was used:

$$T_{gas} = T_{CFD} + \Delta T_{gas} \quad (8)$$

where,

- T_{gas} : main gas path temperature applied to the model
- T_{CFD} : main gas path temperature mapped to ANSYS model points from CFD calculations
- ΔT_{gas} : main gas path temperature offset factor; its nominal value was 0 and, as detailed in section 3.3, it followed a probabilistic distribution function in order to model the gas path temperature variability

The cooling path thermal boundary conditions were obtained using heat transfer coefficient (h_{cool}) and bulk temperature (T_{cool}) at the cooling channel surfaces. The OEM provided the values of h_{cool} and T_{cool} at several points along the cooling passages from 1-D calculations based on cooling airflow variables. The application of cooling parameters at the cooling channel surfaces was performed in ANSYS by means of cooling lookup tables,

where the locations and values of the given parameters (h_{cool} and T_{cool}) were specified and values to be used at any desired point found by interpolation.

As with the main gas path, the heat convection parameters of the cooling path were variable inputs. The cooling air heat transfer coefficient was given by:

$$h_{cool} = h_{1-D} \cdot Fh_{cool} \quad (9)$$

where,

- h_{cool} : cooling air heat transfer coefficient applied to the model
- h_{1-D} : cooling air heat transfer coefficient calculated by interpolation of 1-D estimated points
- Fh_{cool} : cooling air heat transfer coefficient scaling factor; its nominal value was 1 and, its variability followed a probabilistic distribution function

Cooling air bulk temperature was given by:

$$T_{cool} = T_{1-D} + \Delta T_{cool} \quad (10)$$

where,

- T_{cool} : cooling air temperature applied to the model
- T_{1-D} : cooling air temperature calculated by interpolation of 1-D estimated points
- ΔT_{cool} : cooling air temperature offset factor; its nominal value was 0 and, as detailed in section 3.3, it followed a probabilistic distribution function in order to model the cooling path temperature variability

The remainder of the blade surfaces were external surfaces not in contact with the main gas path. These are the side and lower surfaces of the hub platform and the shank. For these, the OEM provided [16] a set of constant heat convective parameters (heat transfer coefficients and bulk temperatures) that were applied through ANSYS thermal sub-model. The bulk temperature for these surfaces was in the order of 750 K. The heat transfer coefficient for platform surfaces ranged between 1200 – 1700 W/m²·K. For shank surfaces it was lower than 100 W/m²·K. The thermal boundary conditions for the hub and shank surfaces were kept unchanged throughout all the probabilistic analysis simulations for each one of the three geometric versions of the blade.

To build the thermal model of the blade volume, the tetrahedral option of SOLID90 element (a 3-D 10-node element) was used (Figure 14).

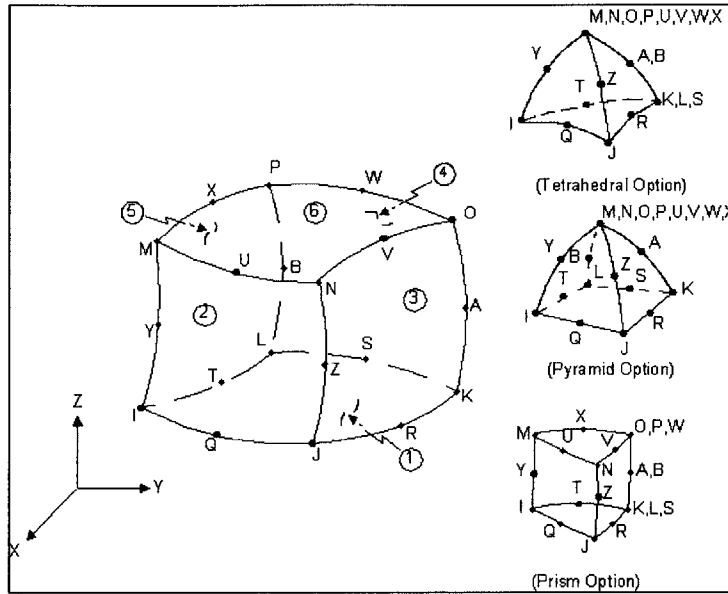


Figure 14 - ANSYS thermal element SOLID90 [18]

The use of a solid element with midpoints was adopted to achieve increased solution accuracy by applying a quadratic solution function. The heat convection thermal load applied in the project is a fully supported surface load for element SOLID90. Each node of the element has a single degree of freedom, temperature.

The rationale for selection of the specific element was its fitness in modeling curved and irregular boundary surfaces – as was the case in the present project model – as well as its compatibility with structural elements for the required connection between thermal and structural sub-models. Figure 15 depicts the Blade-1 thermal model with tetrahedral SOLID90 elements. The meshes for Blade-2 and Blade-3 were similar.



Figure 15 - Blade thermal model solid elements

For the modeling of the thermal barrier coating (TBC) applied on top of the blade surfaces that come in contact with the main gas path, the triangular option of SHELL131 element was used (Figure 16). This is a 3-D layered shell element with in-plane and thru-thickness thermal conduction capability. The element has four nodes with up to 32 temperature degrees of freedom at each node, depending on the number of layers used. In the present project single-layered shell elements were used in lieu of the TBC. The thickness of the layer (l_{TBC}) was an input variable parameter, with a nominal value $l_{TBC}=0.3\text{mm}$.

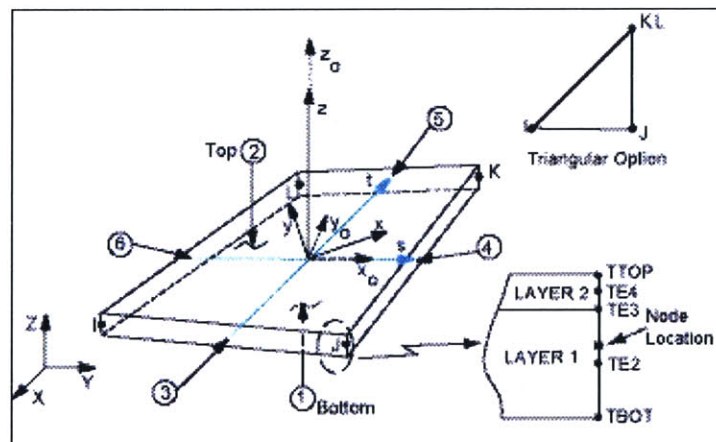


Figure 16 - ANSYS thermal element SHELL131 [18]

The use of the particular shell-type element allowed for the application of the convective heat loads to the outer surface of the airfoil and direct thermal connection with the underlying solid model. A total number of 17008 elements were used in the thermal model; 14930 were tetrahedral volumes modeling the metal continuum, and 2078 were shell elements simulating the TBC.

Appendix A provides an overview of the thermal analysis performed in ANSYS. Figure 17 gives an example of the calculated metal temperature distribution in Blade-1. The temperature plots are non-dimensionalized with respect to the maximum metal temperature calculated for Blade-1 (on the order of $0.7T_m$).

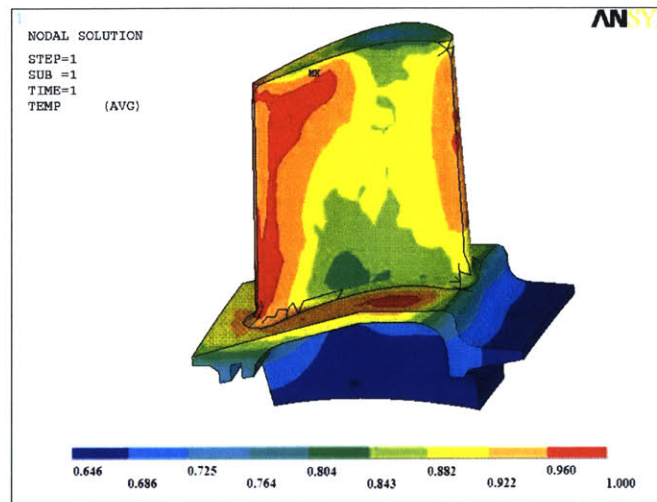


Figure 17 - Thermal analysis output example

With Blade-2 and Blade-3, for comparison reasons the maximum metal temperature of the blades was kept closely (within ± 1 degree) the same as the one in Blade-1 (nominal blade design). To achieve this, the cooling flow was altered. Equations (11) and (12) were used to scale cooling heat transfer coefficients (h_{cool}) and temperatures (T_{cool}) at any point, based on the ratio of cooling air mass flows ($\frac{\dot{m}_{new}}{\dot{m}_{nominal}}$):

$$\frac{h_{cool_new}}{h_{cool_no\ min\ al}} = \left(\frac{\dot{m}_{new}}{\dot{m}_{no\ min\ al}} \right)^{0.8} \quad (11)$$

$$T_{2_new} - T_{1_new} = (T_{2_no\ min\ al} - T_{1_no\ min\ al}) \cdot \left(\frac{\dot{m}_{new}}{\dot{m}_{no\ min\ al}} \right)^{-0.2} \quad (12)$$

In Equations (11) and (12) 1, 2 are sequential points in a given cooling channel, and T_1 , T_2 are respective cooling temperatures at these points. To have the same maximum metal temperature in all three blade configurations, the cooling air mass flow ratio ($\frac{\dot{m}_{new}}{\dot{m}_{no\ min\ al}}$) in Blade-2 was 1.15 and in Blade-3 was 1.3.

To model blade tip cooling (as a result of cooling air coming out of the exits of two cooling channels -A and -B), heat convection boundary conditions were applied on the tip, with heat transfer coefficient from CFD results and the temperatures equal to the temperature of cooling air in the respective cooling channel openings.

3.2.2 Structural Model

The structural FEM analysis used the following inputs:

- a. Thermal load in the form of temperature distribution on the blade metal continuum.
- b. Centrifugal body force $\rho_{metal} \Omega^2 \cdot r$ in the radial direction as a result of the blade rotation ($300 \cdot \pi$ rad/sec).
- c. Pressure loads between pressure and suction sides of the airfoil (transferred from CFD [3]).
- d. Boundary condition of no-displacement for the model nodes in the lowest part of the blade (lower shank zone).
- e. Properties of the material.

The TBC was taken to have no load carrying capability. No transient phenomena were modeled (start-ups or shut-downs).

The thermal and structural analyses used ANSYS-supported feature of *coupled-field analysis* [19], so the thermal analysis results (metal temperature distribution) were applied as body load to the mesh nodes (resulting in isotropic thermal expansion). The pressure was applied at the centroid points of all airfoil external surfaces located element facets. Figure 18 and Figure 19 provide an example of the CFD calculated pressure distribution and the corresponding ANSYS mapped distribution; both were normalized by the average total pressure at the vane inlet [3].

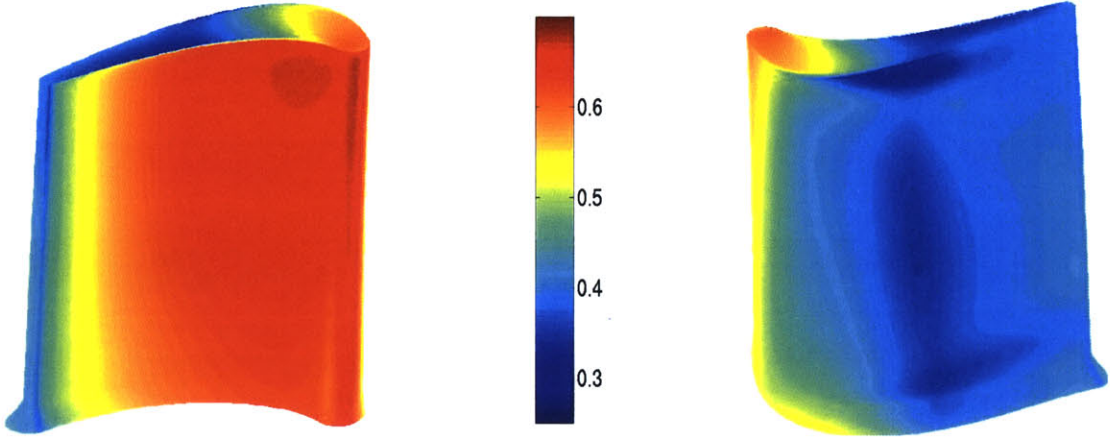


Figure 18 - CFD-generated pressure distribution

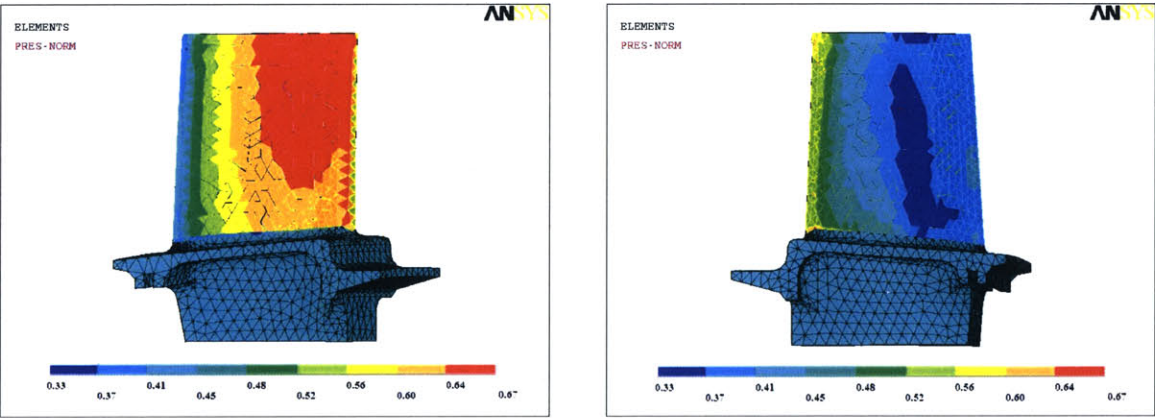


Figure 19 - ANSYS-mapped pressure distribution

The fixed attachment of the blade on the disk is modeled by setting the displacement of all nodes below a specified distance from platform to zero. This was unchanged throughout the study.

The non-linear stress-strain relationships at different temperatures (Figure 10 in Section 3.1.2) were obtained from the ANSYS-provided *Multilinear Isotropic Hardening* (MISO) option, as recommended [20] for large strain including plasticity. MISO option involves the use of a look-up table where temperature dependent stress-strain curves have been input.

Creep-effect was modeled by a two-step process. Initially the loads were applied for a very short period (10^{-5} sec) with the effect of creep not considered. The loading condition was then maintained for longer period, equal to the cycle time of interest (14 hrs). This two-step creep application is recommended by ANSYS documentation [20] since creep strain rate changes significantly during early stage of load application (primary creep). In the second step, creep was described as in Section 2.3 by means of the simplified version of Norton's law exponential form (Equation (6))⁶.

In order to build the structural model of the blade volume in ANSYS, the tetrahedral option of SOLID186 element was used (Figure 20). Details of the meshing are given in Appendix B.

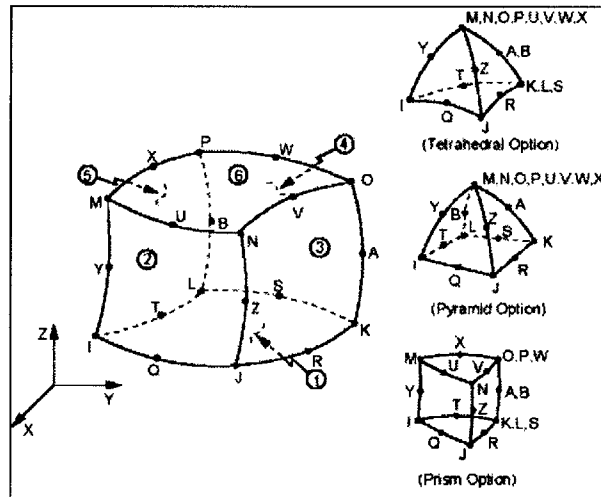


Figure 20 - ANSYS structural element SOLID186 [18]

To give an idea of the grid density, a total number of 16654 tetrahedral SOLID186 elements were used for the structural calculations of Blade-1 (Figure 21 and Figure 22).

⁶ It was modeled in ANSYS by means of *implicit time integration* equation (ANSYS creep equation #9 from [18]), which applies to secondary creep calculations.



Figure 21 - Structural model solid elements - general view



Figure 22 - Structural model solid elements - refined area in region of high stress and strain

From the calculated stress and strain, the *equivalent* (Von Mises) *stress* (σ_{equiv}) and *equivalent* (Von Mises) *strain* (ε_{equiv}) were used in the estimation of fatigue and creep.

The Von Mises stress condition is one of the most widely used plastic flow criterion for metals [5]. Furthermore, it is conveniently applied for design purposes [21] to give a single-value representation of the node stress level. For any specified node, the equivalent stress and strain are defined as follows [21, 22]:

$$\text{Equivalent stress: } \sigma_{equiv} = \left\{ \frac{1}{2} \cdot [(\sigma_1 - \sigma_2)^2 + (\sigma_2 - \sigma_3)^2 + (\sigma_3 - \sigma_1)^2] \right\}^{1/2} \quad (13)$$

where, σ_1 , σ_2 , and σ_3 are the principal stresses.

$$\text{Equivalent strain: } \varepsilon_{equiv} = \frac{1}{1 + \nu'} \cdot \left\{ \frac{1}{2} \cdot [(\varepsilon_1 - \varepsilon_2)^2 + (\varepsilon_2 - \varepsilon_3)^2 + (\varepsilon_3 - \varepsilon_1)^2] \right\}^{1/2} \quad (14)$$

where, ε_1 , ε_2 , and ε_3 are the principal strains, and ν' is the effective Poisson's ratio, or

$$\nu' = \begin{cases} \text{material's Poisson ratio for elastic and thermal strains.} \\ \text{or} \\ 0.5 \text{ for plastic, creep, and hyperplastic strains} \end{cases}$$

It was determined that the location of maximum strain and maximum stress was the bottom of a slot located along the blade TE (Figure 23) and used for cooling air exiting from internal cooling channel-C to the main gas path. This particular area was not modeled exactly as in the original configuration. After being defeatured (Section 3.1.1) the configuration of the cooling slot changed from curved (Figure 24(a)) to rectangle (Figure 24(b)). As a result of the sharp configuration the FEM calculation produced very high stress/strain values in a limited number of elements.

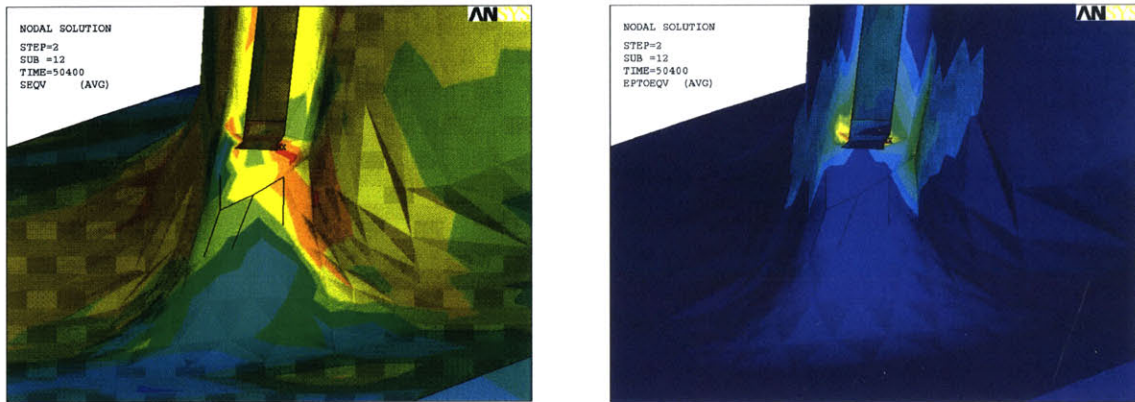
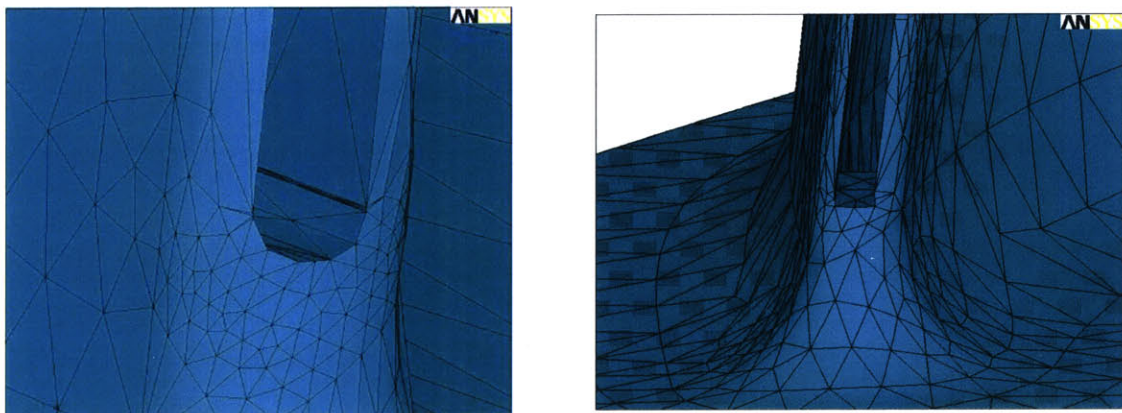


Figure 23 - Maximum stress/strain location



(a) Original

(b) As modeled

Figure 24 - Cooling slot configuration

The singularity was addressed in the calculations by refining the model grid in the subject area, and using the average stress and average strain values for a set of nodes in the subject area. The same convention was applied to the three blades.

The criterion for the nodes selection was to define a volume around the maximum stress/strain location with dimensions related to the physical fracture properties of the material. ASTM Standard E-813 defines an approach to relate material fracture characteristics with dimensions of a part [23]. In brief, the subject standard defines the minimum dimensions of test specimens for the study of elastic-plastic fracture mechanics based on the J-integral approach [5] (J_{IC} testing). The objective is to ensure that the dimensions of a pre-cracked test specimen will have a minimum value required to ensure J-integral condition dominance. Superalloys literature specifies that for intermediate (550 – 750°C) and high temperatures (750°C and higher) where the creep zone around an assumed crack tip is significant, the J-integral approach can be applied [2].

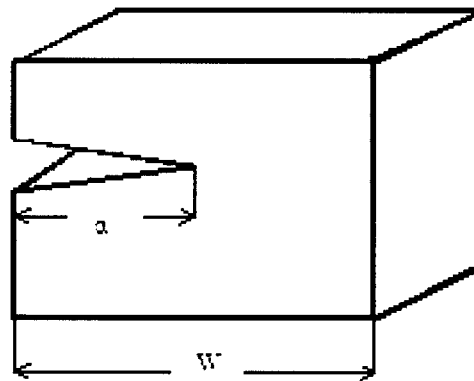


Figure 25 - Pre-cracked test specimen sketch

With reference to Figure 25, the E-813 standard requirements used can be summarized by the following two relations:

$$\frac{\alpha}{W} \geq 0.5 \quad (15) \quad \text{and} \quad (W - \alpha) \geq 25 \cdot \frac{K_{IC}^2}{E \cdot \sigma_y} \cdot (1 - \nu^2) \quad (16)$$

where,

α : Initial crack length

- W : Total specimen width
- K_{IC} : Material fracture toughness
- E : Material elasticity (Young's) modulus
- σ_y : Material yield strength
- ν : Material Poisson's ratio

Due to absence of a K_{IC} value for the modeled alloy (IN-738LC) an approximated value of $100 \text{ MPa(m)}^{1/2}$ was used, based on other superalloy data (133 for IN-706, 96.4 for IN-718 [13] and 90 for IN-903 [24]). By using material properties values for IN-738LC from Table 2, it was calculated that the specimen width for a valid J_{IC} testing should be at least 2.4mm.

A cubic volume of 3mm edge was thus used with the lower cooling slot edge being in the middle of the aft-most side of the cube. The σ_{equiv} and ϵ_{equiv} values at all the FEM model mesh nodes included in the subject volume were averaged and the results ($Avg_ \epsilon_{equiv}$ and $Avg_ \sigma_{equiv}$) were used in the fatigue and creep formulations (equations (4) and (6)) in lieu of ϵ_{tot} and σ_{tot} , respectively. Durability life was calculated in number of 14-hr cycles (N), based on the FEM analysis results ($Avg_ \epsilon_{equiv}$ and $Avg_ \sigma_{equiv}$) by applying Equations (4), (6), and (2) in Chapter 2.

3.3 Probabilistic Analysis

As mentioned previously, the method for assessing the sensitivity of blade durability life to the variability of selected design parameters was to perform Monte Carlo analysis using the thermal/structural model. The actual calculation of durability life was performed using a separate MATLAB⁷ script, and the sample of input and output variables for the 1000 simulations was analyzed statistically using statistical software JMPIN⁸.

Based on inputs from the OEM [25], the noise variables for the present project are given in Table 3 with their respective lower/upper limits:

⁷ The Mathworks, Inc. headquarters, 3 Apple Hill Dr., Natick, MA 01760, <http://www.mathworks.com>

⁸ SAS Institute Inc., Cary, NC 27513, <http://www.JMPdiscovery.com>

	<u>DESIGN PARAMETER</u>	<u>Symbol</u>	<u>Nominal</u>	<u>Lower Limit</u>	<u>Upper Limit</u>
a.	TBC thickness	l_{TBC}	0.3 mm	-10%	+10%
b.	TBC thermal conductivity	k_{TBC}	1 W/m ² ·K	-10%	+10%
c.	Metal thermal conductivity	k_{metal}	18 W/m ² ·K	-10%	+10%
d.	Gas path heat transfer coefficient	h_{gas}	from CFD	-20%	+20%
e.	Cooling heat transfer coefficient	h_{cool}	from 1-D	-20%	+20%
f.	Gas path temperature	T_{gas}	from CFD	-30 K	+30 K
g.	Cooling temperature	T_{cool}	from 1-D	-30 K	+30 K

Table 3 - Probabilistic analysis input design parameters

Note that the heat transfer coefficients (both in main gas and cooling paths) follow different variability pattern than the respective temperature parameters; the variability of coefficients h_{gas} and h_{cool} refer to percentage change of the nominal value (scaling), whereas the one of temperatures T_{gas} and T_{cool} refer to difference in degrees (offset). The technique detailed in section 3.2.1 was adopted for the use of scaling (Fh_{gas} and Fh_{cool}) and offset (ΔT_{gas} and ΔT_{cool}) factors respectively (reference Equations (7) through (10)). Variability of all parameters listed in Table 3 was taken as a normal distribution. The mean and standard deviation for all input variables of the model are summarized in Table 4.

	<u>MODEL INPUT VARIABLE</u>	<u>Symbol</u>	<u>Mean</u>	<u>Std Deviation</u>
a.	TBC thickness	l_{TBC}	0.3 mm	$0.3 \times 0.1 / \Phi^{-1}(0.9)$
b.	TBC thermal conductivity	k_{TBC}	1 W/m ² ·K	$1 \times 0.1 / \Phi^{-1}(0.9)$
c.	Metal thermal conductivity	k_{metal}	18 W/m ² ·K	$18 \times 0.1 / \Phi^{-1}(0.9)$
d.	Gas path heat transfer coefficient scaling factor	Fh_{gas}	1	$0.2 / \Phi^{-1}(0.9)$
e.	Cooling heat transfer coefficient scaling	Fh_{cool}	1	$0.2 / \Phi^{-1}(0.9)$
f.	Gas path temperature offset factor	ΔT_{gas}	0	$30 / \Phi^{-1}(0.9)$
g.	Cooling temperature offset factor	ΔT_{cool}	0	$30 / \Phi^{-1}(0.9)$

Table 4 - Normally distributed random input variables

The quantity $\Phi^{-1}(0.9)$ is the inverse of the standard normal cumulative distribution function at quantile 0.9. The factor $1/\Phi^{-1}(0.9)$ is used to ensure that 90% of the area under the probability density curve lies above the specified lower limit (Table 3), and 10% of the area under the same curve lies above the upper limit (Table 3).

For the probabilistic analysis, 1000 thermal/structural calculations were carried out for each of the three blade design versions. The sample size of 1000 was selected as a compromise between desired accuracy and computational economy with emphasis in the latter. Latin Hypercube Sampling (LHS) was employed to decrease the uncertainty in the probabilistic estimates for the given sample size.

The input/output variable data from the samples was analysed with JMPIN statistics software. The sample of durability life values was analysed for distribution (mean, standard deviation, proximity to normal distribution etc). To identify the sensitivity of durability life to the input variables variability Spearman's rank-order correlation test [26] was used. Spearman's test is a non-parametric correlation method which does not require the assumption of a particular distribution for either the input or the output. The Spearman's rank-order correlation coefficients (ρ) were calculated as

$$\rho = 1 - \frac{6\sum d^2}{n(n^2 - 1)} \quad (17)$$

where n is the number of data points and d is the difference between the rank order of the input parameter and that of any examined output parameter [26]. Values of correlation coefficients can range from -1 to 1 . A value of zero indicates no correlation, a value of 1 strong correlation, and a value of -1 negative correlation

4. Nominal Blade Analysis Results

4.1 Deterministic analysis

The results of a deterministic analysis with all design parameters having their nominal value are provided in the following paragraphs. In the results in Chapters 4 and 5, temperatures have been normalized by nominal blade (Blade-1) maximum temperature, stress and strain results by Blade-1 maximum stress and strain values, respectively, and durability life (N) results (in number of 14-hr cycles) by Blade-1 mean durability life.

The metal temperature distribution in the blade is depicted in Figure 26 and Figure 27.

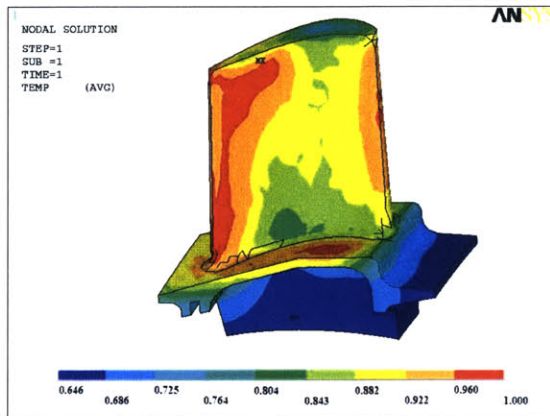


Figure 26 - Blade-1 PS metal temperature distribution

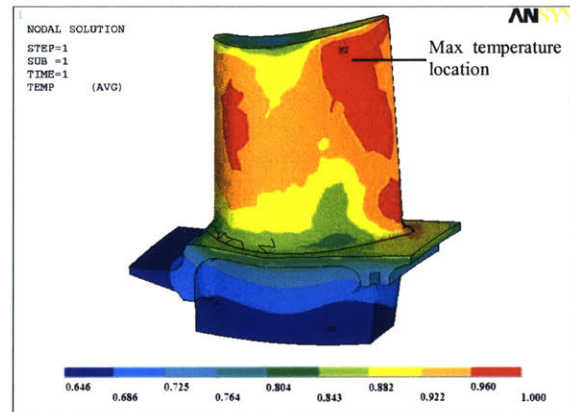


Figure 27 - Blade-1 SS metal temperature distribution

The maximum temperature was at 90-95% span on the suction side close to trailing edge, as seen in Figure 27. In general, the metal temperature was higher close to the trailing edge for both pressure and suction sides. Less extensive hot areas were located on the blade leading edge and on the top surface of the blade platform.

Figure 28 and Figure 29 depict the *equivalent* (Von Mises) *stress* (σ_{equiv}) for the deterministic simulation.

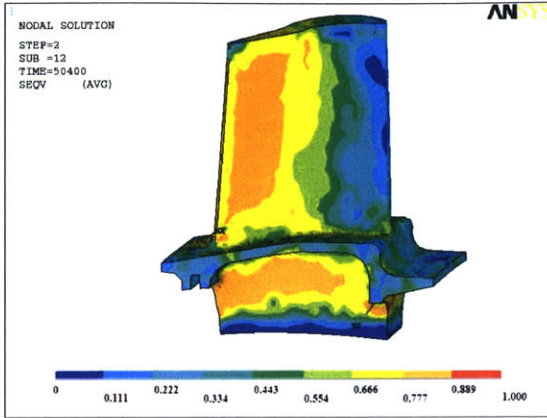


Figure 28 - Blade-1 PS equivalent stress distribution

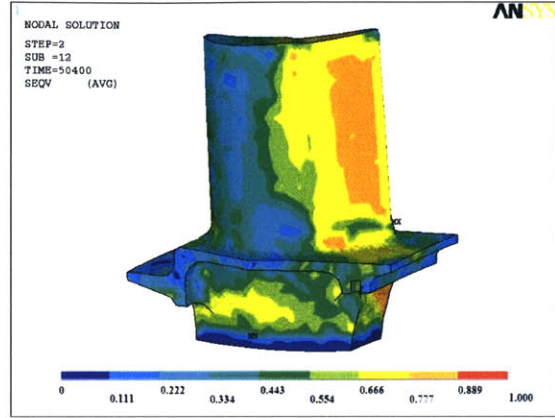


Figure 29 - Blade-1 SS equivalent stress distribution

Blade high stress areas are the aft 40-50% of airfoil pressure and suction sides and the “pressure” side of the blade shank. The maximum stress was in the bottom of the trailing edge cooling slot (Figure 30). The stress levels in all other locations mentioned previously were less than 90% of the maximum value.

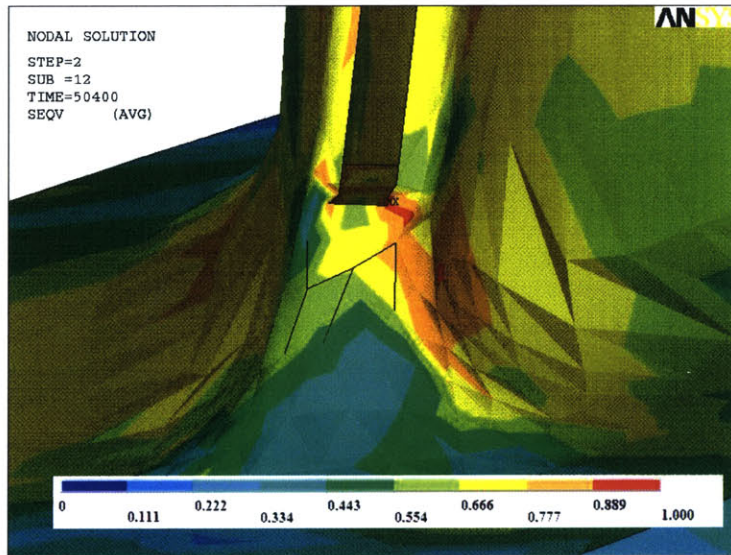


Figure 30 - Stress at Blade-1 life limiting location

Equivalent (Von Mises) strain distributions in Blade-1 (pressure and suction side views, respectively) are plotted in Figure 31 and Figure 32.

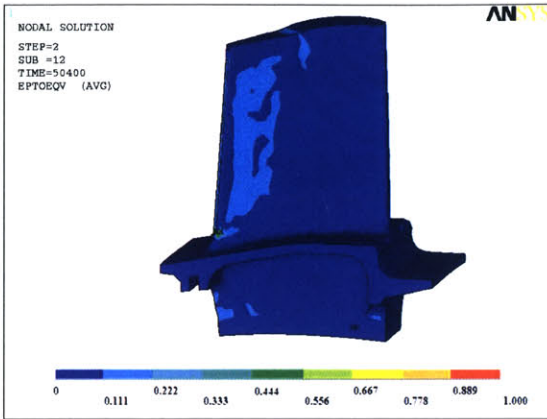


Figure 31 - Blade-1 PS equivalent strain distribution

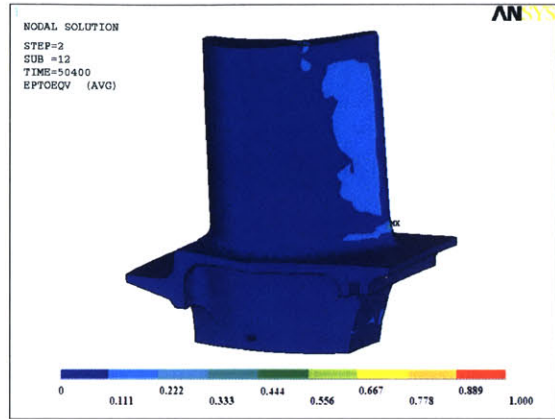


Figure 32 - Blade-1 SS equivalent strain distribution

Areas of high strain are the 30-40% aft part of pressure and suction sides in the airfoil, the forward and aft corners of “pressure” side in the shank and the bottom edge of trailing cooling slot, where the maximum strain value was noted (Figure 33 below). The strain levels in the areas mentioned above are quite low (less than 22.2%) compared with the maximum strain in the blade.

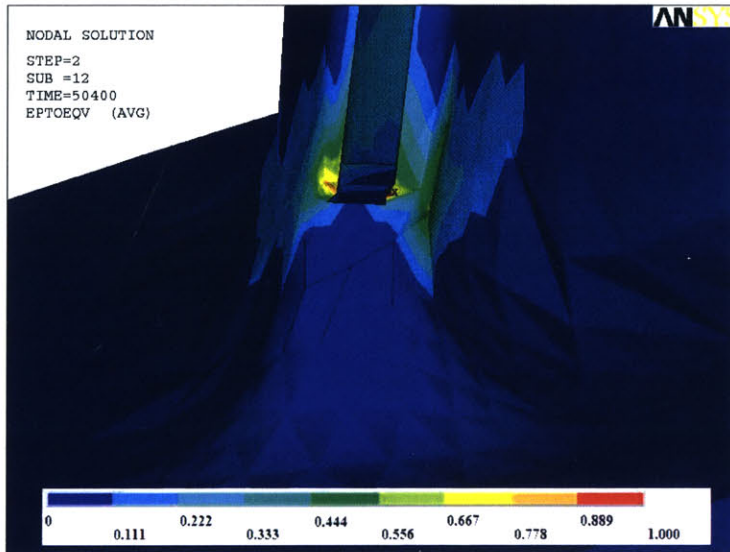


Figure 33 - Strain at Blade-1 life limiting location

The equivalent stress (σ_{equiv}) and strain (ϵ_{equiv}) values were used to estimate the “durability life” at each node. Although there is limited physical meaning of durability life based on stress and strain values at points (nodes), the nodal calculation of “durability life” provides a pictorial representation (Figure 34) of the blade’s weak areas.

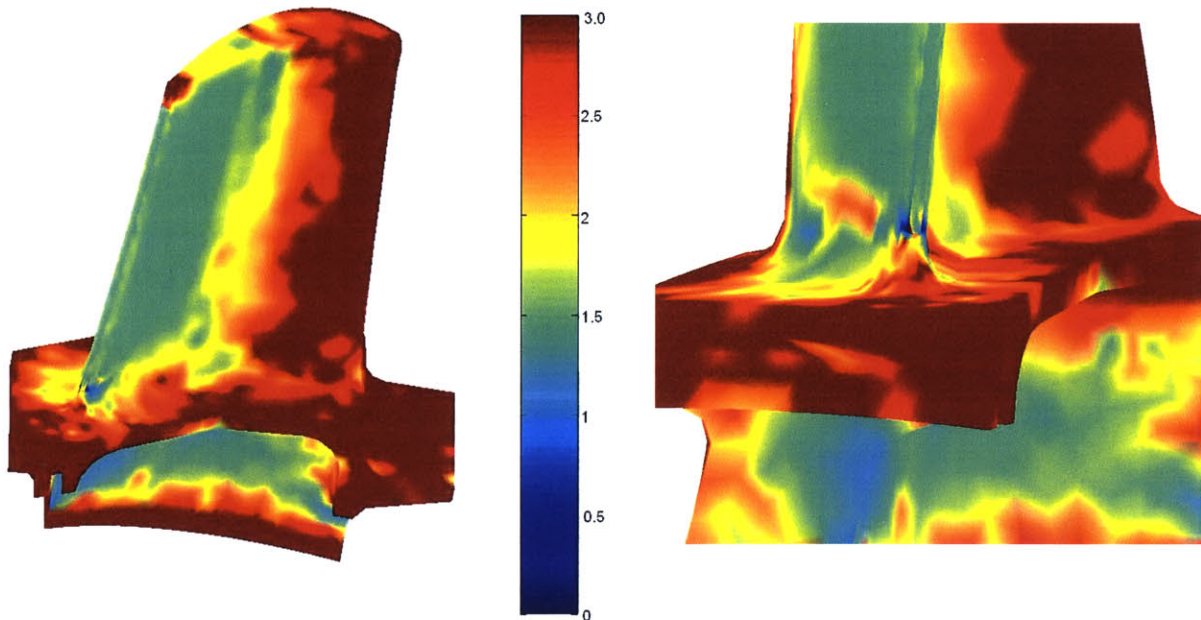


Figure 34 - Blade-1 durability life mapping

The area of lowest durability (darkest blue colored in Figure 34) is the area around the bottom edge of trailing edge cooling slot. The defined this region as the life limiting location of the blade. Fatigue damage accounted for 56 % of the durability life and creep contributed 44 % in linear damage rule (Equation (2)).

To examine in more depth the drivers of durability, an additional deterministic analysis was executed with the whole blade isothermal at 60 K lower than the temperature calculated in the location of interest for the nominal case, and no pressure loads⁹. The durability life was increased by approximately 30% compared to the nominal. Creep-related damage was only 8% of the total damage, since the time-to-creep-rupture was increased by at least one order of magnitude. As can be seen in Figure 35, when temperature decreases the effect of creep is strongly reduced.

⁹ The estimate of creep damage in this case was based on approximated coefficients by correlation from Figure 35.

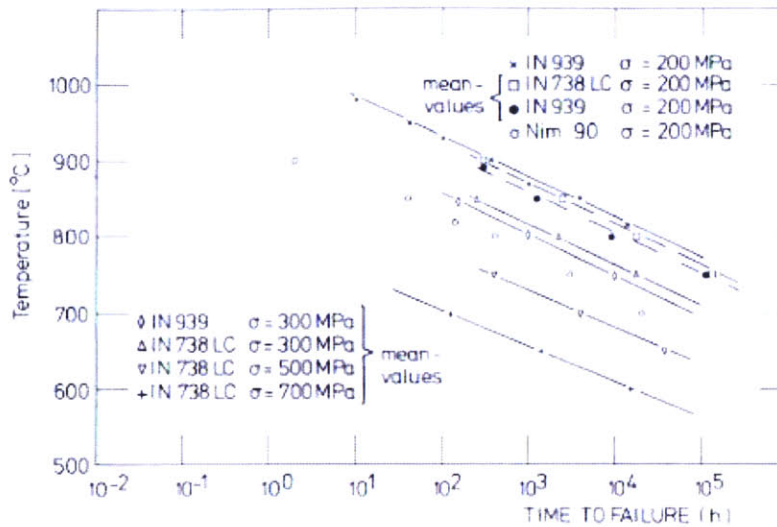


Figure 35 - Iso-stress temperature vs. time-to-creep-rupture plot for various superalloys [9]

Conversely, carrying out an isothermal analysis at a constant temperature of +50 K compared to local metal temperature in the weak area resulted in creep-dominated damage accounting for ~90% of the total damage with the durability life decreased by ~84%.

The effect of modeling of the external flow on durability has been addressed in [3], where it was shown that for the cases studied the differences in metal temperature in the life-limiting location were within ± 5 K. These differences did not affect durability life more than 3% of the nominal value.

To conclude, it could be noted that durability life of the nominal blade is highly dependent on the metal temperature of the location of interest. In the nominal temperature range (within 5-10 degrees of the nominal temperature) durability life is governed, to a large extent, by the loads imposed by the rotation in conjunction with the specific geometric/material configuration of the part. Furthermore, in lower temperatures rotation structural loads dominate entirely and the blade is expected to fail only due to the loads cycling (fatigue). However, if local metal temperature exceeds the nominal value by an order of 5% or more, creep would dominate almost completely and the blade would fail significantly sooner.

4.2 Probabilistic analysis

The durability life distribution for Blade-1 that resulted from the probabilistic analysis is shown in Figure 36. The results are summarized in Table 5.

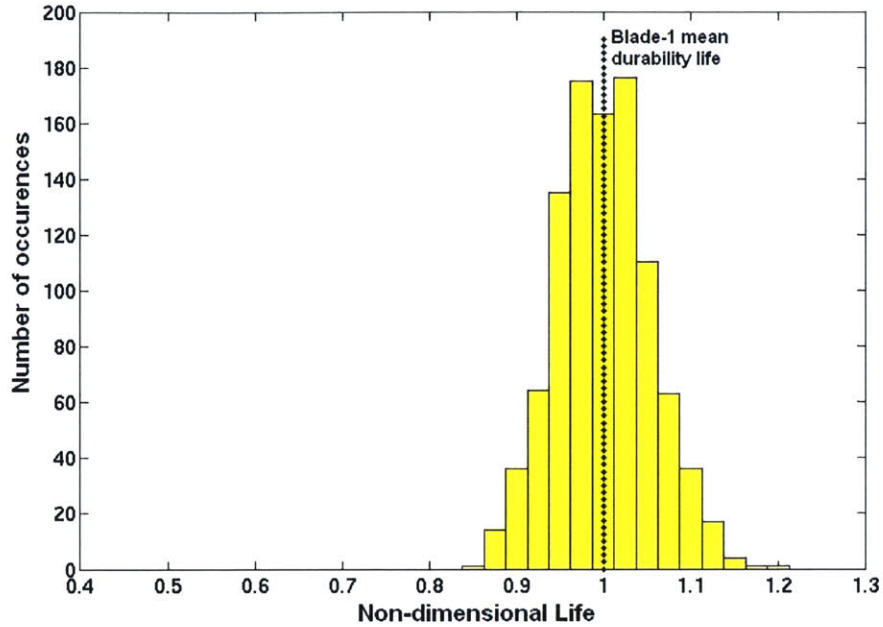


Figure 36 - Blade-1 durability life distribution

Mean	1
Standard Deviation	0.054
Coefficient of Variation	0.054

Table 5 – Blade-1 durability life distribution statistics

As a metric of the *robustness* of each design, it was decided to use the coefficient of variation ($COV_1=0.054$ for Blade-1) and the probability that the durability life is less than 90% of the specific design's deterministic life. Using JMP-IN software, a normal distribution ($\mu_1=1, \sigma_1=0.054$) was fitted to the Blade-1 durability life histogram (Figure 37), with quite satisfactory *Goodness-of-Fit* [27] (Shapiro-Wilk index¹⁰ $W=0.99$). Based on the

¹⁰ The Shapiro-Wilk W statistic is basically the ratio of regression estimate $\hat{\sigma}^2$ to sample variance S^2 . It is similar to R^2 -value and therefore, values close to unity indicate distribution close to normal.

fitted-normal distribution this probability was calculated to be $P(X < 0.9) = 3.2\%$ for Blade-1. Based on the available sample (1000 LHS runs), the probability was estimated as 2.71%.

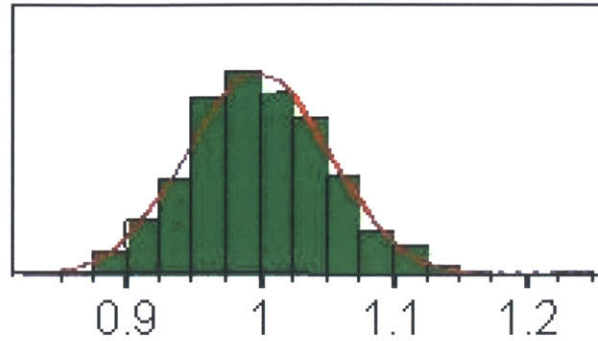


Figure 37 - Normal distribution fitted in Blade-1 data

To indicate the sensitivity of durability life to the input variables variability Table 6 presents the rank-order correlation coefficients between inputs and durability life results of the Blade-1 probabilistic model.

	ρ -coefficient	$P(\rho=0)$
T_{cool}	-0,80	<0,01%
T_{gas}	-0,32	<0,01%
Fh_{gas}	-0,27	<0,01%
Fh_{cool}	0,27	<0,01%
l_{TBC}	0,10	0,14%
k_{TBC}	-0,08	1,09%
k_{metal}	0,0010	97,51%

Table 6 - Blade-1 design input/output correlation coefficients

From the table it can be concluded that the variation of cooling temperature as expressed by cooling temperature offset factor (ΔT_{cool}) has a major impact on the variation in Blade-1 durability. The main gas path temperature (ΔT_{gas}) and heat transfer coefficient (Fh_{gas}) as well as cooling side heat transfer coefficient (Fh_{cool}) have less impact. The other input

variables examined (metal and TBC thermal conductivity and TBC thickness) have correlation coefficients close to zero and/or significant probability that this coefficient is actually zero.

A method to visualize the characteristics of the noise variables that lead to “low” durability life (less than 0.9 of the mean) is to plot the distributions of input variables for the low life subset of the 1000-LHS sample and compare them to the input distributions of the full 1000-LHS sample. The results are presented in Figure 38. The low-life blades occur when the cooling passage temperature is high, and the cooling passage convective heat transfer is low, relative to the nominal values. For most of the other parameters, the distributions of the input variables for the low-life sample are similar to the full-sample distribution, indicating that durability life is not strongly dependent on any particular value of these other parameters. These visualizations are consistent with the Spearman rank correlation coefficient analysis.

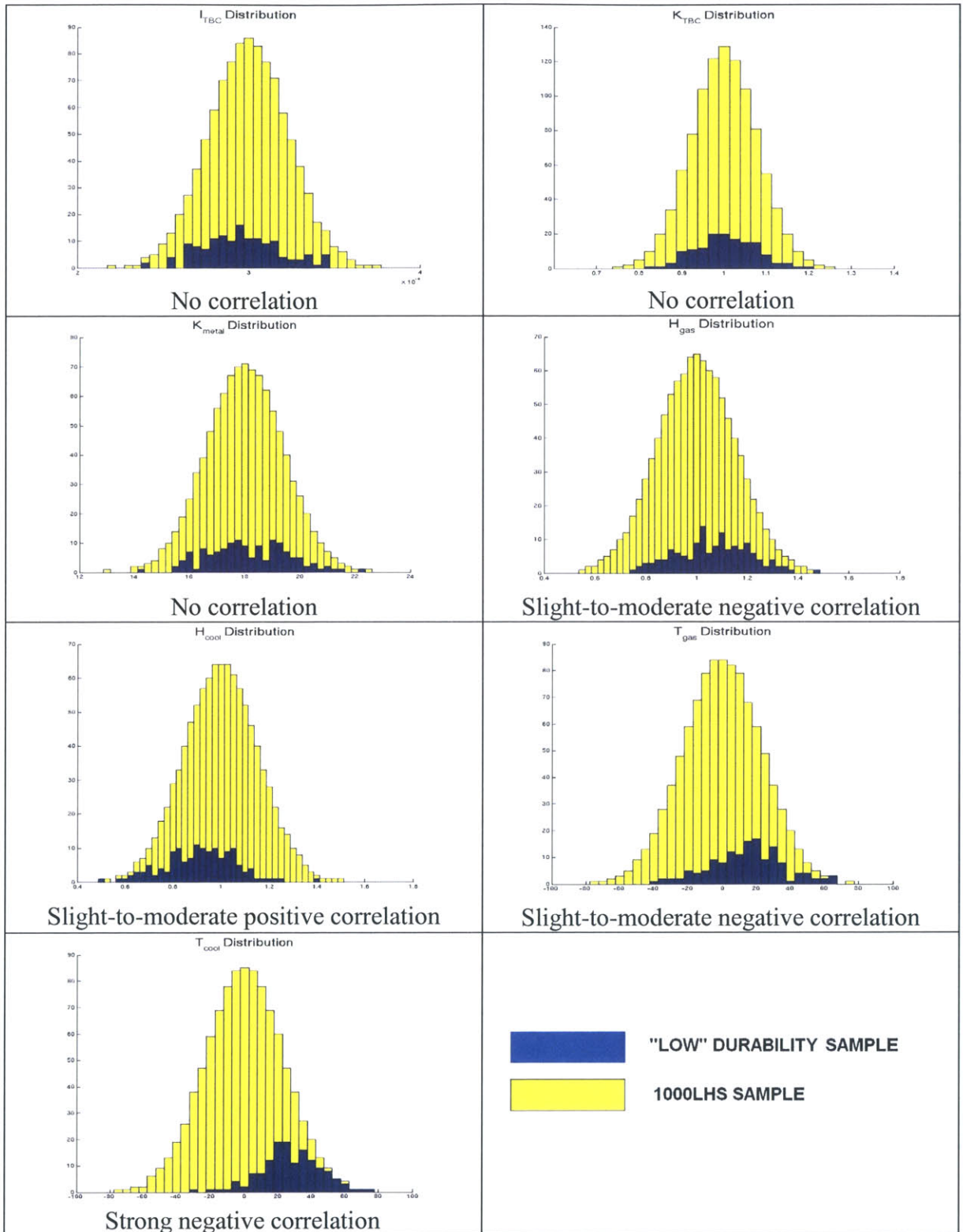


Figure 38 - "Low" life vs. general sample distributions for the seven input variables

5. Blades -2 and -3 Analysis Results and Comparison

5.1 Deterministic analysis

Deterministic analyses were performed for Blade-2 and -3 models. The design parameters were at nominal values. Figure 39 depicts the metal temperature distributions for the three blades¹¹.

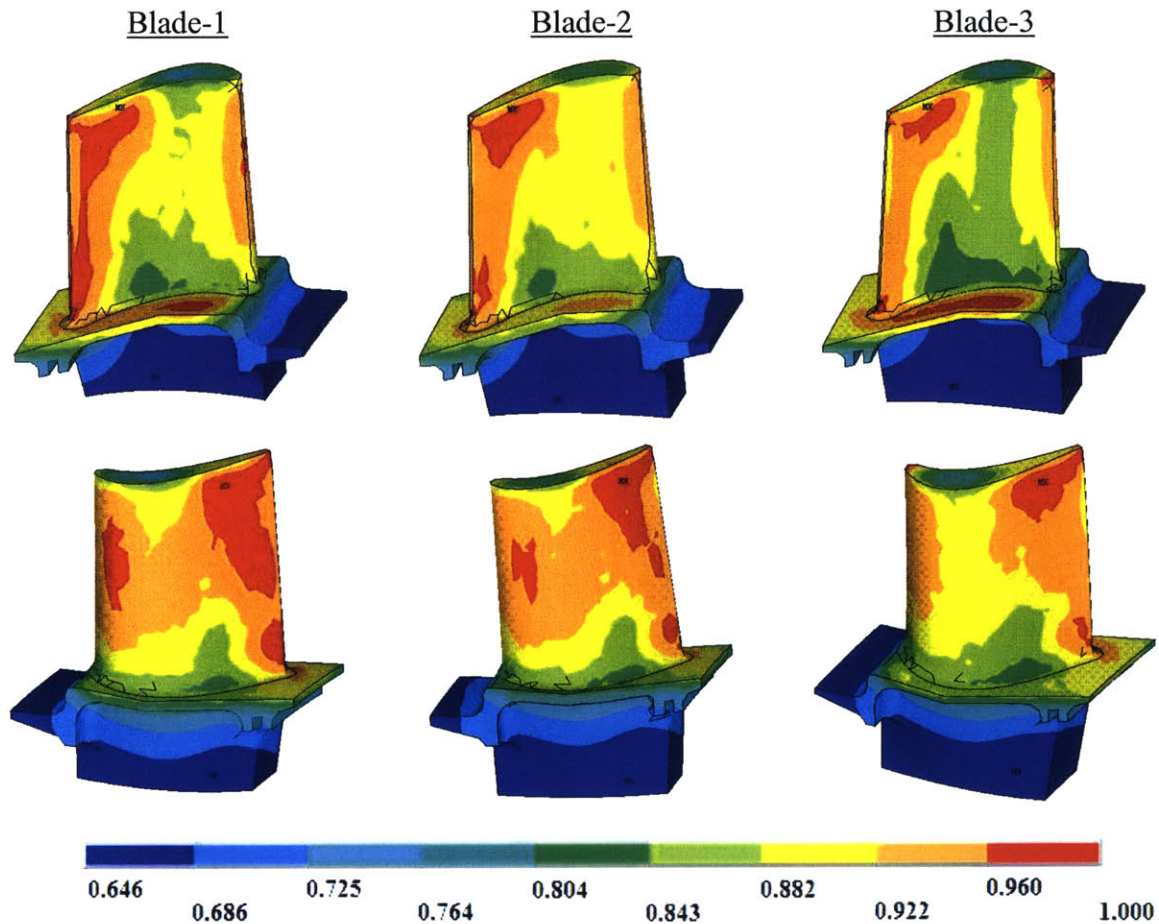


Figure 39 - Metal temperature distributions in all three blade designs

Blade-1 and -2 have generally similar temperature distributions, although Blade-2 has its areas of high temperature range smaller. Over most of the blade, Blade-3 appears

¹¹ As described, Blade-2 and -3 cooling schemes were adjusted by increasing cooling mass airflow so that the calculated maximum metal temperature in both Blade-2 and -3 would be equal (within ± 1 degree) to Blade-1.

even cooler than Blade-2. The hot areas are much reduced. The location of maximum temperature is the same in all three cases. A hot spot is noted in the pressure side of the upper platform surface of all three blade designs; it is more extensive in Blade-3, and less hot in Blade-2. The life limiting location (within 5-10% of trailing edge) is in the same temperature range ($0.96 - 1$ of T_{max}) in all three cases.

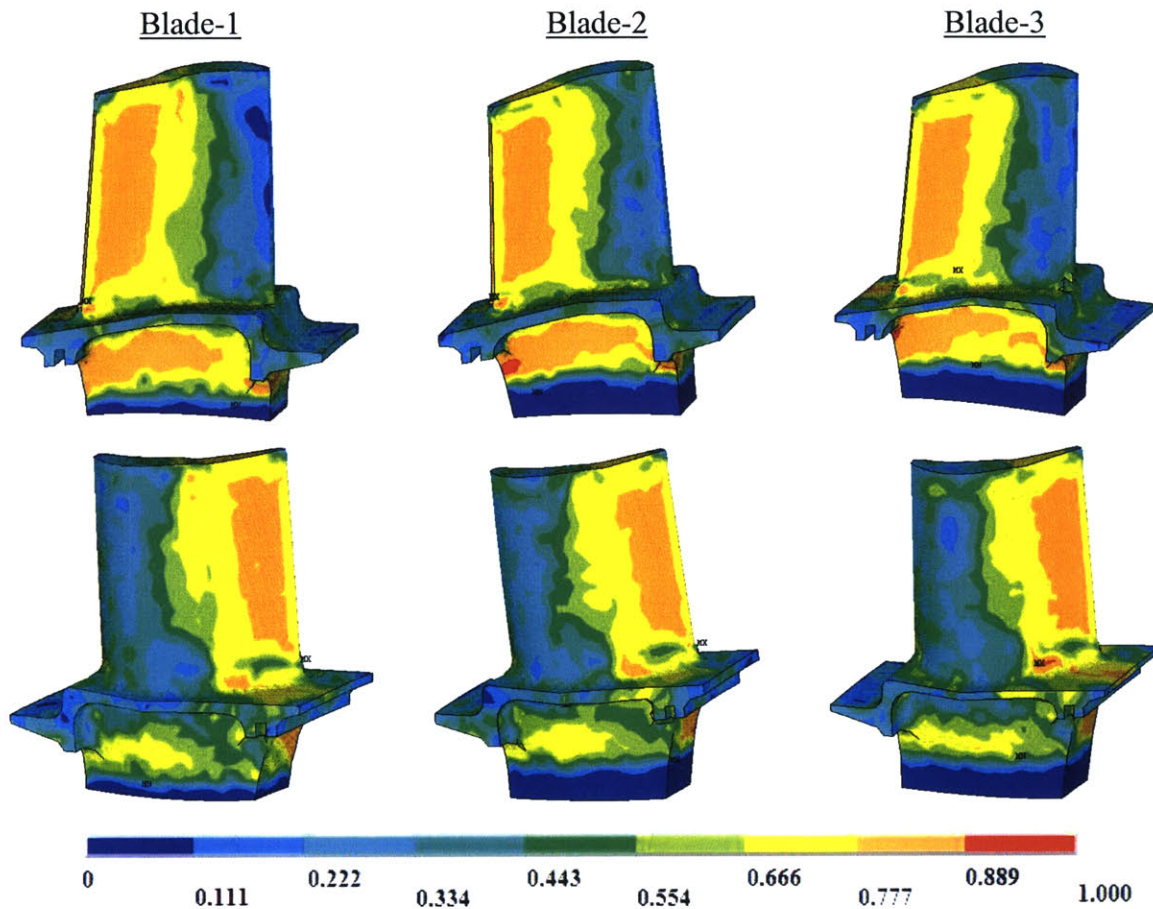


Figure 40 - Equivalent (Von Mises) stress distribution in all three blade designs

Figure 40 shows the *equivalent* (Von Mises) *stress* (σ_{equiv}) distribution for all three blades. The stress has similar distribution in all three blades. The high stress areas are in the region of 60-100% chord on the pressure and suction sides, the pressure side of shank, the bottom of trailing edge cooling slot, and a small area in the airfoil-to-platform fillet suction side. The aft corner of shank pressure side in Blade-2 and -3 has higher stress levels than Blade-1. The location of maximum stress is the same at Blades-1 and -2, the bottom of the

trailing edge cooling slot. In Blade-3 the maximum stress location is at about 5% spanwise (fillet area) of the suction side at 60-70% chord location. The maximum stress in Blade-2 was approximately 7% higher than in Blade-1. In Blade-3 it was almost the same (lower by less than 1%).

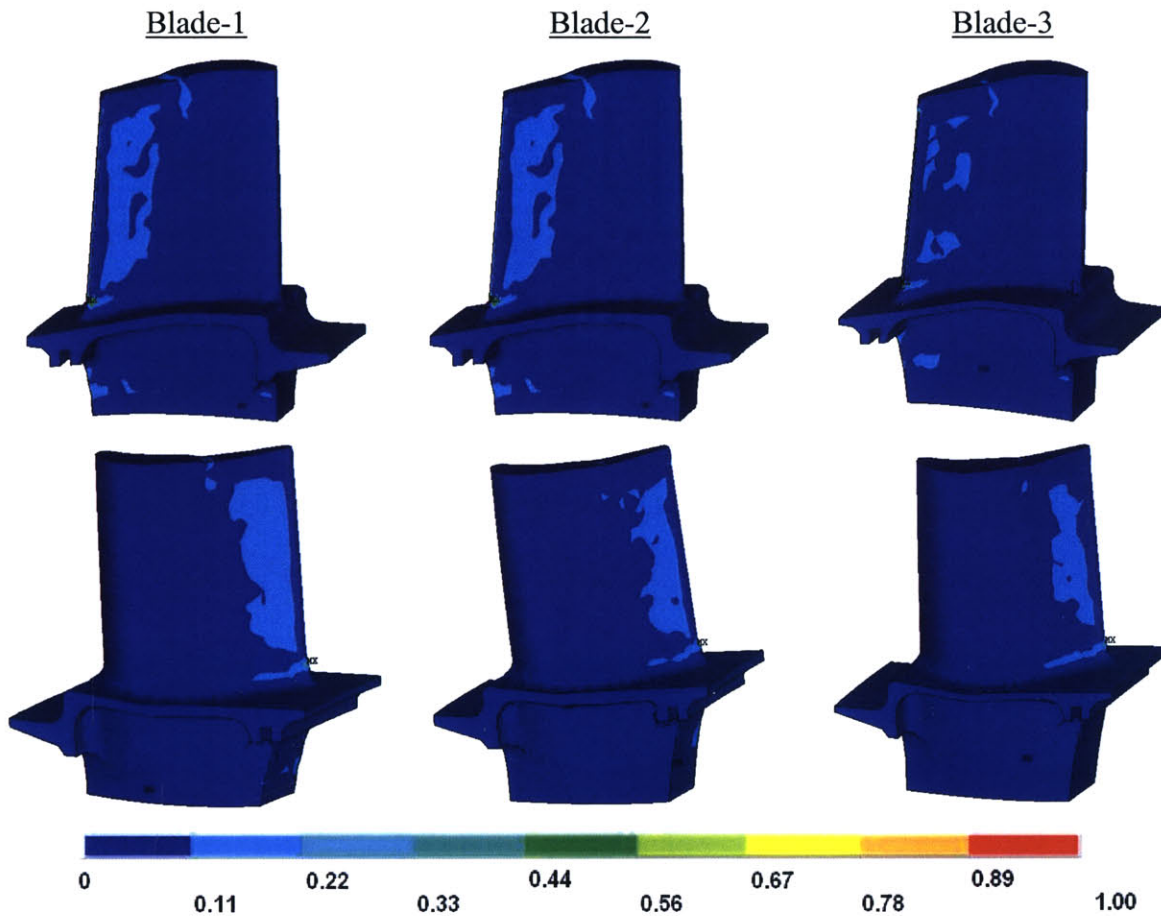


Figure 41 - Equivalent (Von Mises) strain distribution for three blade designs

Figure 41 depicts the *equivalent* (Von Mises) *strain* (ϵ_{equiv}) distributions in Blades-1, -2 and -3. The strain distribution is similar for all three blade design variants. The high strain areas include extended regions in the aft portion of pressure and suction sides, a limited number of spots in the pressure side of shank, and a region extending in the airfoil root forward from the location of maximum strain value (Figure 41). The three blades are not severely strained; in all locations apart from the maximum strain regions strain is less than 22.2% of the maximum. The location of maximum strain is the bottom of trailing edge

cooling slot for the three blades. The maximum strain in Blade-2 is 13% higher than in Blade-1 and in Blade-3 it is 22% higher. Because the Blade-3 overall strain distribution is less severe and the temperature in the location of interest was practically the same as in Blade-1, the higher maximum strain value cannot be related to thermal differences. It is suggested that it could be attributed to local geometric features (such as metal thickness, blade mass distribution etc) although this has not been confirmed.

The location of maximum stress and strain was the same in all three blades with the exception of maximum stress location in Blade-3, which is in the fillet suction side. The life limiting location for the three design variations was the bottom of the trailing edge cooling slot. As seen in the durability life mappings (Figure 42 and Figure 43), the calculated durability life is lowest at the same life-limiting location as for Blade-1.

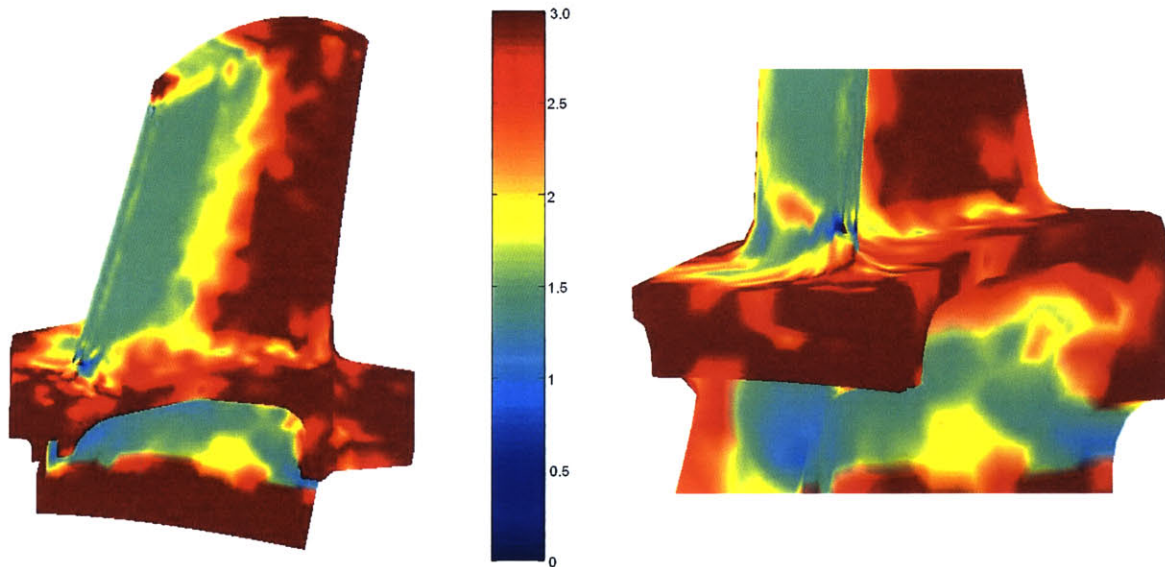


Figure 42 – Blade-2 durability life mapping

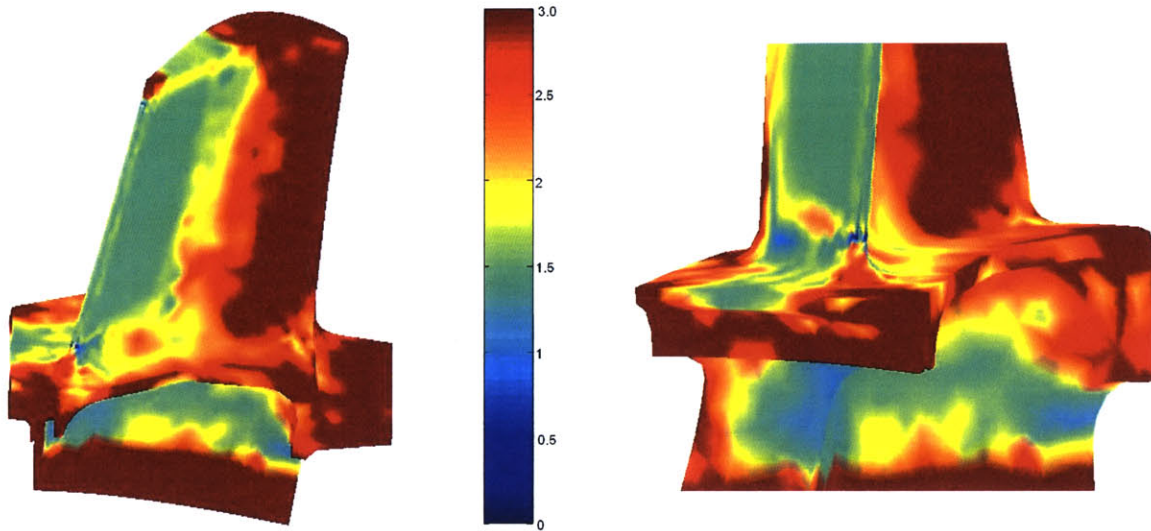


Figure 43 – Blade-3 durability life mapping

The deterministic durability life estimated for Blade-2 was approximately 34% lower than Blade-1, the nominal blade design. For Blade-2, 31% of the damage is attributed to creep. Creep damage is related with material stress level (for further details please see discussion in section 2.3), and the maximum stress in Blade-2 was estimated to be 7% higher than in Blade-1. The remaining 69% of overall damage in Blade-2 is due to fatigue, which is a function of the cyclic strain to the metal. The maximum strain in Blade-2 was higher than in Blade-1 by approximately 13%.

For Blade-3, the durability life was estimated to be approximately 16% lower than for Blade-1. The creep-driven damage was 25%. The fatigue damage index was 75%, with maximum strain having been increased by approximately 22%.

There was no difference in local metal temperature and the implication is that the difference in durability life, at least as modeled, is driven by the centrifugal loads imposed on the different blade geometries.

5.2 Probabilistic analysis

Figure 44 and Figure 45 depict Blade-2 and –3 durability probabilistic life distributions. The life is normalized by the Blade-1 mean life.

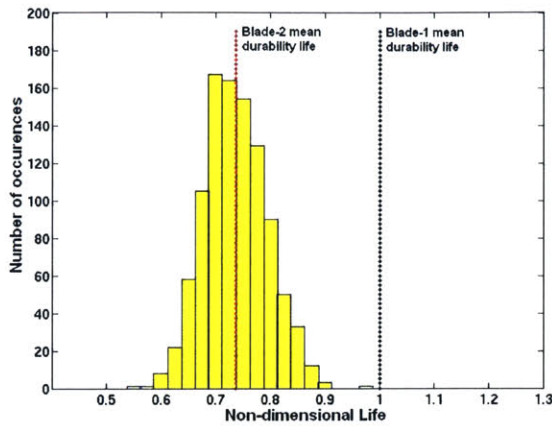


Figure 44 - Blade-2 durability life distribution

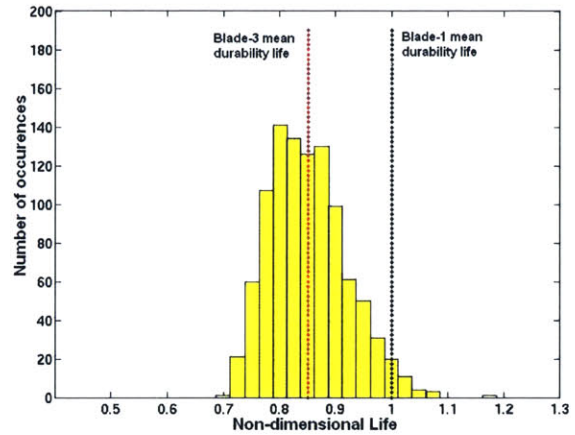


Figure 45 - Blade-3 durability life distribution

Statistics of the probabilistic results for the three blades are summarized in Table 7. The mean values of durability life differ from the respective deterministic runs from –2.34% to 4.7%. It is believed that this is due to the limited number of simulations executed (1000 LHS).

	<u>Blade-1</u>	<u>Blade-2</u>	<u>Blade-3</u>
Deterministic result	1.0243	0.7034	0.8470
Mean	1	0.73647	0.85134
Standard Deviation	0.05365	0.05703	0.06980
Coefficient of Variation	0.05365	0.07743	0.08198

Table 7 – Blades -1, -2, and -3 durability life distribution statistics

Normal distributions fitted to the Blade-2 and –3 probabilistic data, are shown in Figure 46 and Figure 47. Again, the *goodness-of-fit* was quite satisfactory with Shapiro-Wilk test indices $W_{blade-2}=0.99$ and $W_{blade-3}=0.97$.

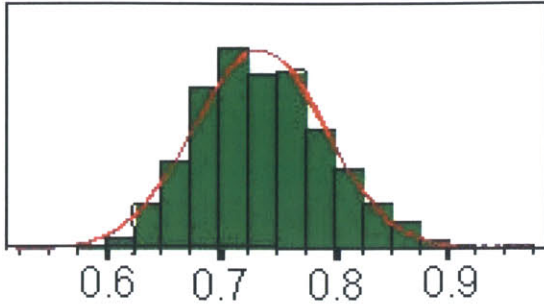


Figure 46 - Normal distribution fitted in Blade-2 data

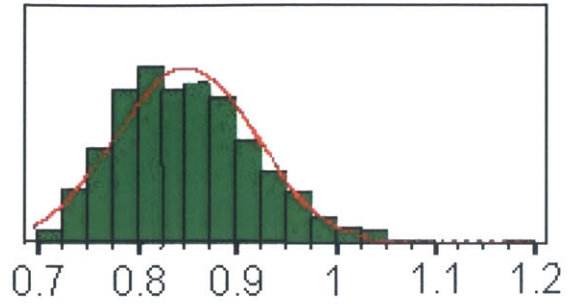


Figure 47 - Normal distribution fitted in Blade-3 data

As a check, the probability of having “low” durability life (less than 0.9 of the mean), using both the fitted distribution and the actual sample results, is provided in Table 8.

	<u>Blade-1</u>	<u>Blade-2</u>	<u>Blade-3</u>
Using fitted distribution	3.14%	9.85%	11.12%
Using sample data	2.71%	9.01%	8.8%

Table 8 - Probabilities for "low" durability life

From coefficients of variation (Table 7) and the probabilities for “low” life (Table 8) the Blade-1 design appears to be more *robust* than Blade-2 and –3. Durability life distributions in Blades –2 and –3 have at least a coefficient of variation at least 50% higher than in Blade-1. They also present as high as 3-times the probability for “low” life (less than 0.9 of the respective mean life) compared to Blade-1 design.

Table 9 presents the rank-order correlation coefficients (Spearman’s coefficients) between inputs and durability life results for all three designs.

	<u>Blade-1</u>		<u>Blade-2</u>		<u>Blade-3</u>	
	ρ -coeff.	$P(\rho=0)$	ρ -coeff.	$P(\rho=0)$	ρ -coeff.	$P(\rho=0)$
l_{TBC}	0,1013	0,14%	0,0694	2,84%	0,0676	3,27%
k_{TBC}	-0,0807	1,09%	-0,0683	3,09%	-0,0535	9,09%
k_{metal}	0,0010	97,51%	-0,0182	56,61%	0,0204	51,98%
Fh_{gas}	-0,2737	<0,01%	-0,2300	<0,01%	-0,2191	<0,01%
Fh_{cool}	0,2671	<0,01%	0,3369	<0,01%	0,2314	<0,01%
ΔT_{gas}	-0,3233	<0,01%	-0,2270	<0,01%	-0,2234	<0,01%
ΔT_{cool}	-0,8000	<0,01%	-0,8155	<0,01%	-0,8839	<0,01%

Table 9 - Variable inputs - durability life rank-order correlation coefficients

The conclusions for the inputs versus durability life correlation in the three designs can be summarized as follows. Cooling side heat convection bulk temperature (ΔT_{cool}) has a negative correlation with the blade durability life. Its absolute value ranges from 0.8 to 0.88 and the probability of it actually being zero is small (<0.01%). Three inputs have a slight-to-moderate correlation with the expected blade durability life. These are: (i) cooling side heat transfer coefficient scaling factor (Fh_{cool}) (positive relation), (ii) main gas path bulk temperature offset factor (ΔT_{gas}) (negative relation), and (iii) main gas path heat transfer coefficient scaling factor (Fh_{gas}) (negative relation). The rank-order coefficients for these inputs have absolute values in the range of 0.22 – 0.34, but there is high confidence they are not equal to zero. The three remaining input variables examined (l_{TBC} , k_{TBC} , and k_{metal}) have little impact on the blade durability life, as their coefficients have values close to zero.

6. Summary and Conclusions

The sensitivity of durability life of three turbine blades, a nominal design, and two design variants, was evaluated with respect to variability of a number of selected design/operating parameters. In order to address the impact of variability on life, probabilistic analyses were performed for all three design variants.

Life limiting effects of LCF and creep only were considered. The formulation of LCF-induced damage was performed by means of the *universal slopes method* (a more applied form of the Coffin-Manson and Basquin relation). For creep modeling, a modified version of Norton's law was used, which related creep-induced damage to the stress applied to the blade during one cycle of loading. Both creep and LCF damages were combined using the linear damage accumulation model.

The stress and strain levels expected in the three blade designs were estimated by means of a model built and run in ANSYS FEM software tool. A simplified geometry blade model was used where thermal and structural boundary conditions were applied, simulating the actual operating environment of the blade. For the main gas path thermal boundary conditions (heat convection conditions) were used. For their simulation, the results of a separate CFD analysis performed in the context of another thesis [3] were transferred to the FEM model.

The life-limiting location was found to be the lower edge of the cooling slot located at the blade trailing edge. This location was the point of maximum levels of both stress and strain for all cases, with the exception of maximum stress for one blade.

Durability life was mainly limited by the effect of fatigue (LCF). Based on the results of deterministic analyses, the fraction of LCF-related damage ranged from 56% to 75% of the overall damage index.

The nominal blade design (Blade-1) had the highest life. The calculations also showed that if the temperature at the life limiting location does not vary significantly the durability life is driven by non-thermal factors, presumably the geometric features. However, if the local metal temperature is increased by 5% or more, creep effects dominate and the part is estimated to fail much sooner.

Of all seven (7) variables design parameters examined, the cooling side bulk temperature had the largest effect on durability life. The statistical analysis showed a strong negative correlation between cooling side bulk temperature and the blade durability life. Cooling side heat transfer coefficient, main gas path bulk temperature, and main gas path heat transfer coefficient had a slight-to-moderate affect on blade life. The main gas heat transfer coefficient and bulk temperature had a negative correlation with life, whereas cooling flow heat transfer coefficient had positive relation. These trends carried through for all three blade designs studied even though they had different levels of deterministically calculated durability life. Based on the statistical analyses performed, the nominal blade design showed not only higher nominal durability life but also less variability, as expressed by the coefficient of variation and the probability of durability life less than 0.9 of the mean.

6.1 Future Work Recommendations

Since the life limiting location appeared in a region where the calculation showed high values of stress and strain in only a few elements, it would be useful to assess the impact of modeling on estimated life. It would be also very beneficial to correlate the results even qualitatively with test and/or field experience. The damage model only considers creep and LCF effects. The inclusion of HCF and environmental effects should be considered; particularly the latter with respect to the impact of corrosion at high temperatures.

Appendices

A. ANSYS Thermal Analysis

The thermal analysis performed by ANSYS is in principal the solution with respect to temperatures of a series of heat flux balance equations between the main gas and the cooling air paths for which the free stream bulk temperatures are known (T_{gas} and T_{cool} , respectively) [22, 28]. An over-simplified 1-D diagram is provided in Figure 48 below.

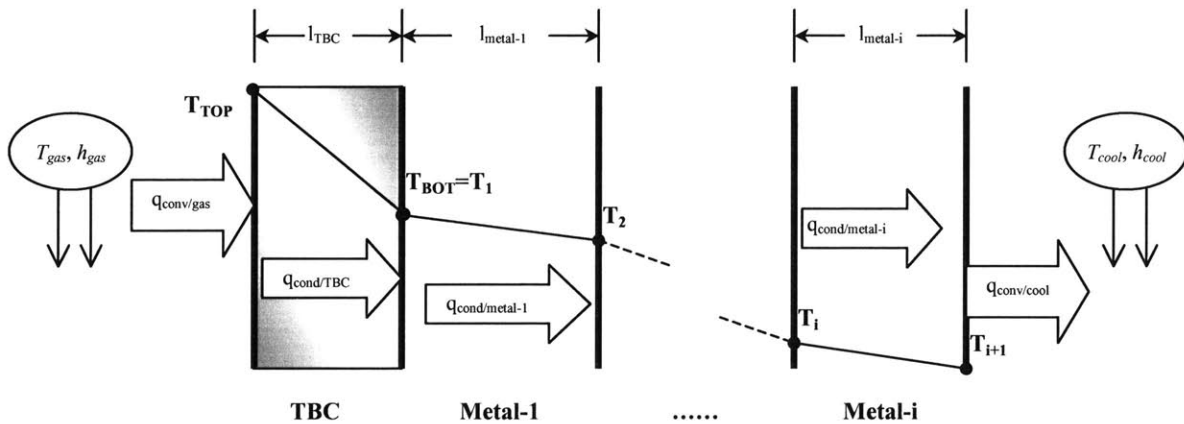


Figure 48 – Simplified 1-D heat transfer diagram

The steady state heat convection model in the main gas and the cooling airflow sides is governed by Newton's law of cooling [28], and thus,

$$q_{conv/gas} = h_{gas} \cdot (T_{gas} - T_{TOP}) \quad (18)$$

$$q_{conv/cool} = h_{cool} \cdot (T_{i+1} - T_{cool}) \quad (19)$$

with q corresponding to heat flux quantities at the examined locations.

For the conductive heat transfer along any given solid part (TBC or metal) Fourier's law holds, or,

$$q_{metal-i/TBC} = -k_{metal-i/TBC} \frac{\partial T}{\partial l_{metal-i/TBC}} \quad (20)$$

From first law of thermodynamics, thermal energy is conserved and, thus:

$$q_{conv/gas} = q_{cond/TBC} = q_{cond/metal-1} = \dots = q_{cond/metal-i} = q_{conv/cool} \quad (21)$$

The solver of ANSYS thermal analysis solves an equivalent system of equations such as (18) through (21) in 3-D and provides the temperature for each node in the mesh.

B. Structural Model Meshing

The used element for structural mesh (SOLID186) is a higher order 3-D 20-node structural solid element. In the tetrahedral option that was used in the project, it has 10 nodes. It provides quadratic displacement solution and it is suitable for modeling of irregular, curved volumes produced by various CAD systems as in the case of the present project. Each node has three degrees of freedom: translations in the nodal x, y, and z directions. Among other non-linear material properties, the element supports plasticity, creep, and large strain capabilities, which were deemed required for the subject structural model. In addition, SOLID186 element is compatible with the solid element used in the thermal sub-model (SOLID90), allowing for the proper transfer of thermal analysis temperature results to structural sub-model nodes.

Although ANSYS provides for automatic meshing control, a more user-controlled approach was selected, in an attempt to find a compromise between the contradictory requirements for small and large elements. The size of the elements had to be small to avoid elements with extremely high or low dihedral angles. Keeping element size limited also prevents abrupt element size reduction in model locations where geometric features require small element modeling.

On the other hand, 3-D modeling of the whole blade requires a high number of elements. However, the overall model run time had to be minimized to allow probabilistic simulations; thus, the total number of elements had to be minimized. After the initial model setup and meshing, test runs were executed during which the location of high stress and strain levels was identified. For that particular location the structural mesh was refined in order to capture with higher accuracy the resulting stress and strain distributions.

Bibliography

1. Kerrebrock, J.L., *Aircraft engines and gas turbines*. 1992, Cambridge, MA: MIT Press.
2. Sims, C.T., Stoloff, N.S., Hagel, W.C., *Superalloys II*. 1987: John Wiley & Sons, Inc.
3. Collin, J.E., *Impact of Aero-Thermal Modeling on the Estimation of Blade Life*, in *Mechanical Engineering*. 2004, MIT: Cambridge, MA.
4. Viswanathan, R., *Damage mechanisms and life assessment of high-temperature components*. 1989: ASM International, Metals Park, OH 44073.
5. Suresh, S., *Fatigue of materials*. 2nd ed. 1998: Cambridge University Press.
6. Fischmeister, H.F., Danzer, R., Buchmayr, B. *Life time prediction models*. in *High temperature alloys for gas turbines and other applications 1986*. 1986. Liege, Belgium: D.Reidel Publishing Company.
7. Bannantine, J., *Fundamentals of metal fatigue analysis*. 1990: Prentice-Hall, Inc.
8. Penny, R.K., Marriott, D.L., *Design for creep*. 2nd ed. 1995: Chapman & Hall.
9. Hoffelner, W. *Creep dominated damage processes*. in *High Temperature Alloys for Gas Turbines and Other Applications*. 1986. Liege, Belgium: D. Reidel Publishing Company.
10. W.F. Brown, L.R.H., *Aerospace Structural Metals Handbook*. Vol. 4. 2000: CINDAS/USAF CRDA Handbooks Operation.
11. ANSYS_Inc, *ANSYS Modeling and Meshing Guide, Release 7.1*. 2003.
12. ASME, *Metals Handbook Vol.1 : Properties and Selection: Iron, Steels, and High-Performance Alloys, 10th ed*. 1990: ASME International Handbook Committee, Metals Park, OH 44073.
13. Donachie, M.J., *Superalloys: a technical guide*. 2002: ASM International, Materials Park, OH 44073.
14. ASM International, *Atlas of Stress-Strain Curves*. 2002: ASM International, Materials Park, OH 44073.
15. Brandes, E.A., Brook, G.B, editors, *Smithells Metals Reference Book*. 7th ed. 1992, Oxford, England: Butterworth-Heinemann Ltd.
16. MHI, *Presentation to MHI-MIT meeting*. 2002.
17. ANSYS_Inc, *APDL Programmer's Guide, Release 7.1*. 2003.
18. ANSYS_Inc, *ANSYS Element Reference Guide, Release 7.1*. 2003.
19. ANSYS_Inc, *ANSYS Coupled-Field Analysis Guide, Release 7.1*. 2003.

20. ANSYS_Inc, *ANSYS Structural Analysis Guide, Release 7.1*. 2003.
21. Barber, J., *Intermediate mechanics of materials*. 2001: McGraw-Hill.
22. ANSYS_Inc, *ANSYS, Inc. Theory Reference, Release 7.1*. 2003.
23. ASTM, *ASTM Standard E-813 for J_{IC} testing*, American Society for Testing Materials, Philadelphia.
24. Moody, N.R., Stoltz, R.E., Perra, M.W, *The effect of hydrogen on fracture toughness of the Fe-Ni-Co superalloy IN903*. Metallurgical Transactions A, 1987. **18A**: p. 1469-1476.
25. MHI, *Presentation to MHI-MIT meeting*. 2003.
26. Sheskin, D.J., *Handbook of parametric and nonparametric statistical procedures*. 2nd ed. 2000: Chapman & Hall/CRC.
27. D'Agostino, R.B., Stephens, M.A., *Goodness-of-fit tests*. 1986, 270 Madison Ave., New York, NY 10016: Marcel Dekker, Inc.
28. Moaveni, S., *Finite element analysis: theory and application with ANSYS*. 2003, Upper Saddle River, NJ 07458: Pearson Education, Inc.